Annu. Rev. Nucl. Part. Sci. 1994. 44:329–71

CHARMONIUM FORMATION IN $p\bar{p}$ ANNIHILATIONS[1]

R. Cester

I.N.F.N. and Department of Experimental Physics, University of Turin, via Pietro Giuria 1, 10125 Torino, Italy

P. A. Rapidis

Fermi National Accelerator Laboratory,[2] P.O. Box 500, Batavia, Illinois 60510

KEY WORDS: resonance, potential model, perturbative QCD, storage ring, gas jet target.

CONTENTS

[1] The US Government has the right to retain a nonexclusive, royalty-free license in and to any copyright covering this paper.

[2] Operated by the Universities Research Association under contract no. DE-AC02-76CHO3000 with the US Department of Energy.

1. INTRODUCTION

In the late 1960s the experimental study of deep-inelastic lepton-nucleon scattering revealed that nucleons can be interpreted as composites of nearly free elementary constituents (partons). This interpretation led to the hypothesis that the strength of hadronic interactions could change with energy from the low-energy regime of "infrared slavery," where constituents are inescapably bound within the hadron, to a high-energy regime of "asymptotic freedom," where the interaction between constituents becomes progressively weaker. Soon after it was shown (1) that a class of renormalizable field theories, invariant under the transformations of a nonabelian gauge group, exhibits this ultraviolet asymptotic behavior. To this class of theories belongs quantum chromodynamics (QCD), which is based on the color SU_3 gauge group and is at present considered a viable theory of strong interactions.

In this context, the discovery (2) of the J/ψ and ψ' states of charmonium in the fall of 1974 was of crucial importance. The observation of these positronium-like bound states of a heavy quark-antiquark pair ($\bar{c}c$) was necessary to establish the credibility of the then nascent idea of asymptotic freedom in QCD. Furthermore, the subsequent observation of a Coulomb-like spectrum of charmonium states[3] established (4):

> ". . . charmonium as the 'hydrogen atom' of strong interaction physics. For it then became possible to subject the gauge theories of strong interactions to fairly stringent tests in a reasonably simple setting. Much of hadronic physics could then be related to charmonium spectroscopy as molecular spectra are related to that of hydrogen."

These early words have indeed turned out to be almost prophetic: A veritable flood of charmonium inspired theoretical investigations[4] (5), and lattice gauge calculations (6) have since appeared in the physics literature.

The earlier studies of charmonium states and their decays were conducted almost exclusively at e^+e^- colliders. In such experiments, the electron-positron annihilation proceeds primarily through an intermediate virtual photon, creating a bound quark-antiquark charmonium state.

[3] For a review of the early e^+e^- experiments see Ref. 3.

[4] The quarkonia bibliography is immense. A convenient collection of many of the more significant theoretical papers is Ref. 5.

This production mechanism limits the quantum numbers of the final states to those of the photon, i.e., $J^{PC} = 1^{--}$. Thus the orthocharmonium states $J/\psi[1^3S_1]$ and $\psi'[2^3S_1]$, as well as the $\psi(3770)[1^3D_1]$ state[5] are readily produced as narrow resonances in e^+e^- collisions. The major advantage of studying the formation of charmonium resonances, by e^+e^- annihilation is the high peak yield relative to the underlying hadronic continuum. The ratio for these processes is ~300 at the J/ψ and ~120 at the ψ'. Precise measurements of the mass and width of these states can be obtained from the energy of the electron and positron beams that are accurately known.

States such as the paracharmonium $\eta_c[1^1S_0]$ and $\eta_c'[2^1S_0]$ or the orbitally excited states $\chi_{c0}[1^3P_0]$, $\chi_{c1}[1^3P_1]$, $\chi_{c2}[1^3P_2]$, and $h_c[1^1P_1]$ cannot be directly produced by e^+e^- annihilation, but they can be studied through the cascade decays of the ψs (e.g., $\psi' \rightarrow \gamma\chi_{c2} \rightarrow \gamma\gamma J/\psi$ or $J/\psi \rightarrow \gamma\eta_c \rightarrow \gamma K\bar{K}\pi$). Consequently, the precision of the measurement of the mass and width of these states has been limited by the resolution of the detector rather than the knowledge of the energy of the beams. In addition, states for which the cascade from the ψ' involves unfavorable branching ratios or multiple steps (e.g. $\psi' \rightarrow \gamma\eta_c'$ or—even worse—$\psi' \rightarrow \gamma\eta_c' \rightarrow \gamma\gamma h_c$) have remained unobserved or poorly studied.

An alternate way to produce and study charmonium is through proton-antiproton annihilation. This process differs from electron-positron annihilation in two important ways. First, the composite nature of the proton (and of the antiproton) allows direct formation of all charmonium states, i.e. one is not limited to $J^{PC} = 1^{--}$ states. Second, the combination of a large nonresonant cross section for the process $p\bar{p} \rightarrow$ hadrons (~70 mbarn) and of the rather small cross-sections for $p\bar{p} \rightarrow (c\bar{c})$ (~1 μbarn at best) leads to a very unfavorable signal to noise ratio. Thus, even though the suggestion of using this alternate method was proposed quite early (7), the realization of such experiments had to await a significant technological advance: the advent of stochastic cooling of stored antiproton beams.

Stochastic cooling (8) is a technique designed to decrease the phase space of stored beams. Its development was the significant step toward the successful operation of high-energy proton-antiproton colliders (9). A direct result of this development was the availability of dense beams of stochastically cooled $\bar{p}$s with precisely controlled momentum and

[5] We use the usual spectroscopic notations $n^{(2S+1)}L_J$, where n is the principal quantum number, which is equal to one plus the number of nodes in the radial wave function, and L, S, and J are the orbital, spin, and total angular momentum of the quark-antiquark system, respectively. For a fermion-antifermion system the parity is given by $P = (-)^{(L+1)}$ and the charge conjugation parity by $C = (-)^{(L+S)}$.

extremely narrow momentum spread ($dp/p \sim .01\%$). In 1979 it was realized (10) that such a beam, with the appropriate energy to form a charmonium resonance, impinging on a stationary hydrogen target, provided all the necessary ingredients for a successful experiment. The precisely defined momentum and the narrow momentum spread of the antiproton beam allowed for excellent resolution in the initial state, which in turn allowed for a precise and direct measurement of the mass and width of charmonium resonances. Furthermore, it was recognized that by selecting charmonium decays into electromagnetic final states, either a high-mass e^+e^- pair or a high-mass pair of γs, one could observe a signal even in the presence of a ferocious nonresonant hadronic background.

Two experiments to date have studied charmonium production in $p\bar{p}$ annihilation: R704 at CERN (11) and E760 at Fermilab (12). Both experiments incorporate the features outlined in Ref. 10. A stochastically cooled beam of antiprotons of variable but well-controlled momentum and of a small momentum spread circulates in a storage ring. The target is a molecular-cluster hydrogen gas jet operating perpendicular to the beam. The stochastic cooling system preserves the beam's emittance and compensates for the small energy loss inside the target, thus providing a beam with constant energy, small energy spread, and long lifetime. This process results in optimal utilization of the antiprotons, which are very costly to produce.

The excitation curve for a charmonium resonance is obtained as a function of the center-of-mass energy for processes such as

$$p\bar{p} \rightarrow (c\bar{c}) \rightarrow e^+e^-, \qquad 1.$$

$$p\bar{p} \rightarrow (c\bar{c}) \rightarrow J/\psi X \rightarrow e^+e^-X, \qquad 2.$$

and

$$p\bar{p} \rightarrow (c\bar{c}) \rightarrow \gamma\gamma, \qquad 3.$$

where $(c\bar{c})$ is a charmonium resonance that decays into the indicated final state. These final states can be efficiently identified, even in the presence of the large nonresonant background, by using a detection apparatus that includes a large-acceptance electromagnetic calorimeter and a Cherenkov counter together with charged-particle hodoscopes and tracking. In addition, the implementation of a two-arm trigger logic that accepts events with e^+e^- or $\gamma\gamma$ that are almost back-to-back in the center of mass (a characteristic of a decay of a high-mass state) further reduces the dominantly hadronic background. From the study of the excitation curve one can determine the mass (M_R), total width (Γ_{tot}), and product of the branching ratios $B_{p\bar{p}}B_f$ of the charmonium

state into the initial ($B_{p\bar{p}} = \Gamma_{p\bar{p}}/\Gamma_{\text{tot}}$) and final states (e.g. for a $\gamma\gamma$ final state, $B_f \equiv B_{\gamma\gamma} = \Gamma_{\gamma\gamma}/\Gamma_{\text{tot}}$). With the excellent resolution in the center-of-mass energy, one can measure directly the total width of even the J/ψ, the narrowest charmonium state.

2. THE ANNIHILATION SOURCE

The characteristics of the annihilation source (instantaneous luminosity, energy definition and control, source dimensions, etc) determine the quality of an experiment of this type. In Sections 2.1–2.3 we first describe in some detail the R704 setup to emphasize the novelty of the approach. In Section 2.4 we summarize the distinctive features of E760 that led to an improvement in source performance over R704.

2.1 *The Beam*

In a formation experiment, in which antiprotons interact on a stationary hydrogen target, the energy of the beam is related to the value of the mass of the resonance

$$E_{\bar{p}} = \frac{M_R^2}{2m_p} - m_p, \qquad 4.$$

where m_p is the mass of the proton. To study the formation of charmonium states in the mass range $2950 \leq M_R \leq 3850$ MeV/c^2 one needs a beam of momentum ranging from 3.6 to 6.9 GeV/c.

When R704 was proposed, there was no antiproton storage ring operating in this momentum range. It was suggested that, with some modifications, one of the CERN Intersecting Storage Rings (ISR) could be used (13). When the ISR were operated as a $\bar{p}p$ collider, particles of opposite charge were transferred to the two ISR after they had been accelerated in the Proton Synchrotron (PS) to a momentum of 26 GeV/c. For R704, on the other hand, the 3.5-GeV/c beam from the Antiproton Accumulator (AA) was transferred to ring 2 of the ISR without acceleration in the PS. To increase transfer efficiency, the large-emittance antiproton beam from the AA was extracted in three successive slices then recombined in a single pulse by the ISR momentum cooling system. The maximum number of antiprotons stored for R704 was $N_{\bar{p}} = 1.1 \times 10^{11}$.

The ISR radio-frequency (RF) system was not sufficiently powerful to capture the low-energy beam, and shortly after injection the beam lost its bunched structure. The antiprotons were then brought to the chosen energy by phase-displacement acceleration, a method applicable to unbunched beams (14). Because the beam emittance deteriorated significantly during acceleration, further cooling was necessary before data taking could begin.

Transverse betatron cooling and momentum cooling were available in ring 2 of the ISR for high-energy operation and were easily adapted to low-energy operation by adding variable delay lines to each system. Vertical betatron cooling was used to combat the vertical blowup of the antiproton beam caused by multiple scattering in the traversals of the target. The momentum cooling system was essential because it reduced the spread of the beam momentum after injection and after acceleration and compensated for the energy loss in the target (~20 MeV/day), thus holding the beam momentum constant during data taking. The momentum cooling system also served as a horizontal betatron cooling system. The minimum relative rms momentum spread obtained was $\sigma_P/P = 4 \times 10^{-4}$ for a 4-GeV/c momentum beam. This value corresponded to a rms spread in the center-of-mass energy ($E_{\rm cm} \equiv \sqrt{s}$) of the $\bar{p}p$ system of

$$\sigma_{E_{\rm cm}} = \frac{m_p}{E_{\rm cm}} \times \beta_{\bar{p}} \times \sigma_P \approx 0.5 \text{ MeV}. \qquad 5.$$

Typical beam transverse dimensions were ~5 mm in height and ~10 mm in width.

Phase-displacement acceleration was used to change the beam energy during a resonance scan. The minimum step, obtained by a single RF sweep, corresponded to a beam-momentum change of 3–6 MeV/c. Smaller energy drifts were obtained by appropriate changes in the momentum stochastic cooling system.

2.2 *The Target*

A molecular cluster gas-jet target (15) is a natural choice for this type of experiment because it can be operated in an accelerator environment and provides a well-localized target of the appropriate density. The target built for the R704 experiment was operated at a density of $\rho_{H_2} = 1.0 \times 10^{14}$ atoms/cm^3 and had a thickness of $d_{H_2} = 0.9$ cm. This target led to a maximum instantaneous luminosity

$$\mathcal{L}_0 = \rho_{H_2} \times d_{H_2} \times N_{\bar{p}} \times f = 3 \times 10^{30} \text{ cm}^{-2}\text{s}^{-1}, \qquad 6.$$

where $N_{\bar{p}}$ is the number of antiprotons circulating in the ring and f is their revolution frequency ($f \approx 3.1 \times 10^5$ Hz).

Figure 1 shows the target arrangement. It depicts, from left to right, the production stage, the accelerator beam pipe crossed by the jet, and the sink stage, where the hydrogen is absorbed. The first element of the production stage is the expansion chamber, from which molecular hydrogen kept at liquid nitrogen temperature ($T_0 = 77$°K) and at a

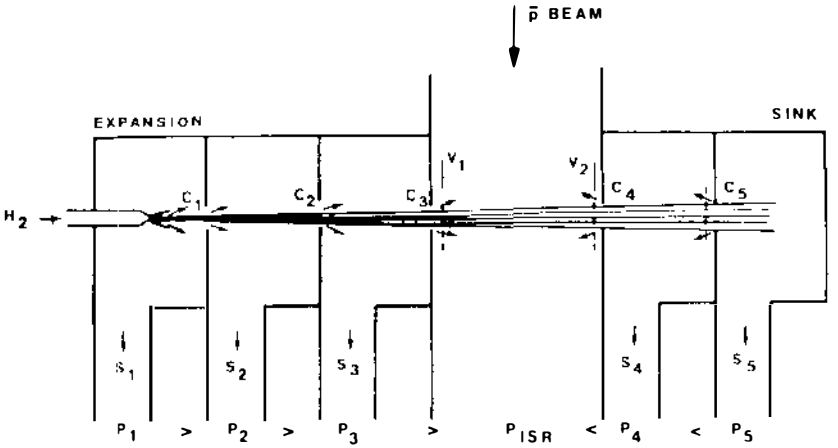

Figure 1 Schematic of the R704 target system (13): Chambers 1, 2, and 3 are the production stage and chambers 4 and 5 are the sink stage. The gas jet intersects the antiproton beam at 90°.

typical pressure of 10 bar escapes through a narrow-throat (30 μm), trumpet-like nozzle. During the adiabatic expansion, large molecular clusters (10^4–10^6 molecules per cluster) are formed in the jet core and flow at high speed (1290 m s^{-1}) over long distances in vacuum. The flow field is similar to that from a point source with almost straight streamlines. Downstream from the nozzle, a three-collimator system selects the central dense part of the jet.

Of a total flux from the nozzle of 10 torr liter s^{-1}, the collimator system selected a target beam of 0.15 torr liter s^{-1} = 10^{19} atoms s^{-1}. A differential pumping system was used to remove the diffuse halo of hydrogen around the jet core. On the sink side the jet was dumped into a large cryogenic pump. During target operation, the pressure increase in the beam vacuum pipe close to the target (caused by the breakup of clusters hitting the walls of the last collimator) corresponded to $\leq$1.5% of the target thickness spread over a few meters.

2.3 *Beam-Energy Measurements*

The velocity of antiprotons circulating in a storage ring can be expressed in terms of the revolution frequency f and the orbit length L_{orb} by

$$v_{\bar{p}} = L_{orb} \times f. \qquad 7.$$

Hence, the total beam energy is

$$E_{\bar{p}} = \frac{m_{\bar{p}}c^2}{\sqrt{[1 - (f \times L_{\text{orb}}/c)^2]}}. \quad 8.$$

The beam-revolution frequency spectrum can be determined by analyzing the beam-current Schottky noise (16). The spectral power density of the Schottky noise is proportional to the particle density at that frequency. The maximum in the frequency spectrum defines L_{orb}, which must be determined independently. L_{orb} is the sum of the ring circumference (central orbit) L_0 and a correction term that measures displacements from the central orbit.

The momentum of the beam on the central orbit can also be determined from the measurement of the magnetic field in the dipoles (B_{dip}):

$$P_{\bar{p}}(\text{GeV}/c) = 0.2997 \times B_{\text{dip}} \times \rho(\text{Tesla} \times \text{m}), \quad 9.$$

where ρ is the bending radius in the dipoles.

Using Equations 7 and 9, one can determine the beam momentum by measuring two of the three variables f, B_{dip}, and L_{orb}. The operational characteristics of the storage ring dictate which of the observables are chosen.

In the ISR experiment the beam momentum was obtained by measuring the revolution frequency and the dipole field (17). The error in this measurement was dominated by the error in the dipole field and was estimated to be $\sigma_P = \pm 1.0$ MeV/c.

An absolute calibration of the beam energy was performed by analyzing the excitation curve at the energy corresponding to the formation of the J/ψ. The energy of the antiproton beam ($E_{\bar{p}}$) at the peak of the excitation curve is related to the mass of the J/ψ by Equation 4, and the uncertainty on $E_{\bar{p}}$ is

$$\Delta E_{\bar{p}} = (M_{J/\psi}/m_{\bar{p}}) \times \Delta M_{J/\psi}. \quad 10.$$

Because the mass of the J/ψ is known from independent measurements to $\sigma_{M_{J/\psi}} = \pm 100$ keV, the corresponding rms error on the beam energy is $\sigma_{E_{\bar{p}}} = \pm 330$ keV. These inputs translate to the error on M_{R}:

$$\sigma_{M_{\text{R}}}(\text{MeV}) = [m_{\bar{p}}/M_{\text{R}}] \times \sqrt{\sigma^2_{E_{\bar{p}}} + [\sigma_P/\beta_{\bar{p}}]^2}. \quad 11.$$

For example, for $M_{\chi_2} = 3.556$ MeV/c,[2] this gives an error $\sigma_{M_{\text{R}}}$(MeV) = 274 keV. To this systematic error one must add the statistical uncertainty in the determination of the peak energy of the excitation curve. This statistical component was by far the dominant one in the ISR experiment, which accumulated only ~3.0 pbarn^{-1} in the few months

of data taking before the ISR was closed and turned into a storage ring for LEP magnets.

Despite its short lifetime, the R704 experiment reported measurements of the mass and widths of the $\chi_{1,2}$ states far superior to previous measurements from e^+e^- collider experiments and demonstrated the effectiveness of the method. A continuation of this line of experiments was called for.

2.4 *The Fermilab Annihilation Source*

The E760 experiment was proposed in 1985 to continue the study of charmonium states formed in $\bar{p}p$ annihilations using the Accumulator of the Antiproton Source at Fermilab. The Accumulator had been designed to store and cool 8.85 GeV/c antiprotons for the Tevatron collider. To provide antiprotons over the range of 3.5–7.0 GeV/c for use in E760, the Accumulator had to be operated in a nonstandard mode. It was first run in its design mode to accumulate the required number of antiprotons at 8.85 GeV/c. The $\bar{p}$ beam was then decelerated to the desired energy (18).

An RF cavity operating at the second harmonic of the beam revolution frequency ($f \approx 0.62$ MHz) and with a maximum RF amplitude of 3 kV was used to decelerate the beam. The deceleration process was controlled by an auxiliary front-end computer that set the current of magnets as a function of beam momentum. The deceleration proceeded at ~20 MeV/s.

After deceleration, the resonance was scanned by changing the beam energy in small steps. The smallest step size was determined by the least significant bit of digital control of the dipole power supply and corresponded to a beam-momentum change of ~150 keV/c. The main dipole and quadrupole power supplies were regulated to one part in 10^5 to ensure excellent stability of the beam orbit and energy.

The Accumulator ring was equipped with powerful transverse and momentum stochastic cooling systems (19) that continuously compensated for the effects of multiple scattering and dE/dx loss in the target and in the residual gas in the ring. The momentum cooling narrowed the center-of-mass energy spread $\sigma_{E_{cm}}$ to ~0.2 MeV. A set of movable pick-up electrodes for momentum cooling made it possible to cool the beam at any chosen radial orbit position.

The internal hydrogen gas-jet target, which was similar in design to the one used in the ISR experiment[6], was operated at a typical density of 0.6×10^{14} atoms/cm^3 and had a diameter of 6.3 mm (for 95% contain-

[6] The E760 target used turbomolecular rather than cryogenic pumps.

ment). The antiproton beam had a diameter of ~5 mm for 95% containment. The peak luminosity achieved was $\sim 1.0 \times 10^{31}$ cm^{-2} s^{-1}, with an antiproton beam of 3.5×10^{11} $\bar{p}$'s. The beam lifetime was 50–90 h, depending on the energy of the beam, and each store was used for ~1–2 lifetimes. During the J/ψ and ψ' formation runs, the relatively high-production cross sections made it possible to complete an energy scan of a resonance within a single store, whereas for low-rate processes such as $\bar{p}p \rightarrow \eta_c \rightarrow \gamma\gamma$ or $\bar{p}p \rightarrow h_c \rightarrow J/\psi\pi^0$, data were accumulated at a single energy for the complete store.

In E760 the beam energy was determined by measuring the orbit length L_{orb} and the beam-revolution frequency. From Equation 8 we derive

$$\Delta E_{\bar{p}} = m_{\bar{p}}c^2 \times \gamma_{\bar{p}}^3 \times \beta_{\bar{p}}^2 \times \left[\left(\frac{\Delta f}{f}\right)^2 + \left(\frac{\Delta L_{\text{orb}}}{L_{\text{orb}}}\right)^2\right]^{1/2}. \quad 12.$$

The revolution frequency was measured precisely ($\sigma_f/f \sim \pm 1.5 \times 10^{-7}$), and the error in $E_{\bar{p}}$ was dominated by the uncertainty in the measurement of the orbit length L_{orb}. The length of the central orbit L_0 obtained from survey measurements was not accurate enough to determine the beam energy with the required precision. The orbit length was therefore calibrated using the precisely known mass of the ψ'.

The orbit length at the peak of the resonance is given by $L_{\text{orb}} = c\beta/f$, where f is measured at this orbit and β is calculated from the ψ' mass. The error ΔL_{orb} in the length of this reference orbit and the error in the reference mass ΔM_{R} are related by the equation

$$\frac{\Delta L_{\text{orb}}}{L_{\text{orb}}} = \frac{M_{\text{R}}}{\gamma^3\beta^2 m_p^2}\,\Delta M_{\text{R}}, \quad 13.$$

where we have neglected the contribution of the error in the beam frequency. The factor γ^3 in the denominator justifies the choice of the ψ' rather than the J/ψ for calibration because for the higher mass state one obtains a better determination of the orbit length for the same ΔM_{R}. The ± 0.1 MeV/c^2 uncertainty in the published (20) mass of the ψ' corresponds to an uncertainty in the L_{orb} of ± 0.67 mm at the ψ'. An orbit length rms error of $\sigma_{L_{\text{orb}}} = \pm 0.67$ mm in turn corresponds to $\sigma_{M_{\text{R}}} = \pm 0.033$ MeV/c^2 at the J/ψ.

Having established a reference orbit at the ψ', one can determine the center-of-mass energy at the other resonances. If one could confine the beam to the reference orbit at all energies, the only error in a measured mass would be the one discussed above. However, the beam cannot be controlled to this precision over the entire energy range of the experi-

Table 1 Comparison of beam and target parameters in R704 and E760

Parameter	R704	E760
Maximum number of $\bar{p}$ stored	1.1×10^{11}	4.0×10^{11}
Jet density (atoms/cm^3)	1.0×10^{14}	0.6×10^{14}
Source dimensions (hor $\times$ vert $\times$ long) cm^3	$1.0 \times 0.5 \times 0.9$	$0.5 \times 0.5 \times 0.6$
Maximum instantaneous luminosity (cm^{-2}s^{-1})	3.0×10^{30}	1.0×10^{31}
Minimum rms E_{cm} spread (keV) at E_{cm} = 4.0 GeV	500	160
Error on χ_2 mass from energy measurements (keV)	274	120

ment. The orbits differed in length from the reference orbit by an amount δL ranging from $+2$ to -2 mm.

The difference between the reference orbit and the orbit used during a resonance scan was measured using 48 horizontal beam-position monitors (BPMs)[7]. The BPM reading at the energy of interest was compared with the BPM reading at the reference energy. The resulting difference in the orbit was used to calculate δL. The error in the orbit length measurement was calculated to be ± 1 mm (21) and corresponded to a mass error of $\sigma_{M_R} = \pm 0.05$ MeV/c^2 at the J/ψ. From these considerations the systematic error on the χ_2 mass for E760 is 120 keV, where contributions from δL and the mass uncertainty of the ψ' have been included. In Table 1 we compare the beam and target parameters for the two experiments.

3. EXPERIMENTAL TECHNIQUE

3.1 *Analysis of a Resonance Excitation Curve*

The charmonium states are studied by sweeping the antiproton energy across a resonance R and measuring the cross section as a function of the beam energy. The resonance parameters are extracted by an analysis of the resulting excitation curve. The observed excitation curve is the convolution of the Breit-Wigner cross section for the resonance with the energy distribution function of the beam, i.e.

$$\sigma(E_{cm}) = \int_0^\infty \sigma_{BW}(E')G(E' - E_{cm})dE', \qquad 14.$$

[7] R704 used B_{dip} rather than L_{orb} for energy determination because BPM measurements require a bunched beam. At the ISR, the beam was not bunched except for a short period after injection, whereas in the E760 experiment the beam could be totally or partially bunched at any energy.

where $G(E)$ is the normalized beam-energy distribution function in the center-of-mass frame. The area under the resonance is given by

$$A = \int_0^\infty \sigma(E_{cm}) dE_{cm} = \frac{\pi}{2} \sigma_{peak} \Gamma_R, \quad 15.$$

which is independent of the form of $G(E)$. σ_{peak} is the cross section at $E_{cm} = M_R c^2$ given by

$$\sigma_{peak} = \frac{12\pi\hbar^2 B_{in} B_{out}}{(M_R^2 - 4m_p^2)c^2}, \quad 16.$$

where B_{in} and B_{out} are the branching ratios ($B = \Gamma_{partial}/\Gamma_R$) in the resonance formation channel ($R \rightarrow \bar{p}p$) and in the decay channel, respectively.

The resonance parameters to be extracted from a complete analysis of the excitation curve are the mass M_R, the total width Γ_R, and the product of branching ratios $B_{in} \times B_{out}$. If $G(E_{cm})$ is unknown, the product $\sigma_{peak}\Gamma_R$ can be obtained from the integral of Equation 15. If $G(E_{cm})$ is known, Γ_R can be directly determined from the analysis of the shape of the measured excitation function, even if the resonance is substantially narrower than the center-of-mass energy distribution. With a beam width $\Gamma_{E_{cm}}$ [full width at half maximum (FWHM)] $\approx$500 keV (as was achieved in E760), Γ_R can be directly determined from the analysis of the shape of the resonance excitation function, even for the J/ψ resonance ($\Gamma_R \approx 100$ keV). The sensitivity to such small resonance widths can be explained as follows: For a beam-energy distribution that is a Gaussian with width $\Gamma_{E_{cm}} (= (8 \ln 2)^{1/2} \sigma_{E_{cm}})$, the measured peak cross section σ^*_{peak} is

$$\sigma^*_{peak} = \sigma_{peak} \sqrt{\frac{\pi}{8}} \frac{\Gamma_R}{\sigma_{E_{cm}}} \exp\left(\frac{\Gamma_R^2}{8\sigma^2_{E_{cm}}}\right) \operatorname{erfc}\left(\frac{\Gamma_R}{\sqrt{8}\sigma_{E_{cm}}}\right), \quad 17.$$

where erfc is the complementary error function. If $\Gamma_{E_{cm}} > \Gamma_R$, one can show that

$$\frac{\sigma^*_{peak}}{A} \simeq \frac{0.94}{\Gamma_{E_{cm}}} \left(1 - 0.94 \frac{\Gamma_R}{\Gamma_{E_{cm}}}\right), \quad 18.$$

where 0.94 is the factor $(4 \ln 2/\pi)^{1/2}$. With $\Gamma_R/\Gamma_{E_{cm}} \approx 0.2$ at the J/ψ, Γ_R can still be directly determined if σ^*_{peak}/A is measured.

The ratio σ^*_{peak}/A is independent of the efficiency and acceptance of the detector and of the absolute value of the luminosity; thus Γ_R can be determined without a detailed knowledge of these quantities. However,

stable running conditions, an accurate knowledge of the beam-energy distribution function, and high statistical accuracy in the data are required.

The measurement of the process

$$\bar{p}p \rightarrow (\bar{c}c) \rightarrow \bar{p}p \qquad 19.$$

for any $(\bar{c}c)$ charmonium state would be desirable because one can extract from the measurement of σ_{peak} a value of $B_{p\bar{p}}$ ($B_{\text{in}}B_{\text{out}} = B^2_{p\bar{p}}$). This measurement is extremely difficult because the process (Equation 19) competes with a large background from $\bar{p}p$ elastic scattering. It has been argued (22) that $B(R \rightarrow \bar{p}p)$ could be extracted from a careful study of interference effects between the process of Equation 19 and the elastic scattering process. This method has not yet been pursued, and at present one depends on other experiments to extract separate values for B_{in} and B_{out}.

Interference between the amplitude for resonant production and the amplitude for continuum, i.e. nonresonant, production of the same final state poses a problem when the two processes are of comparable magnitude. Fortunately, for most of the charmonium states studied, the resonant production is much larger than the continuum, and interference effects are negligible.

At each of the energy points at which data were collected, the measured number of events n_i was fitted to the expected number

$$\nu_i = \mathcal{L}_i[\sigma_{\text{bkg}} + \epsilon\sigma(E_{\text{cm},i})], \qquad 20.$$

where $\sigma(E_{\text{cm}})$ is the cross section given by Equation 14 and σ_{bkg} is the background cross section. $\mathcal{L}_i$ is the luminosity for the data taken at the ith point, and ϵ is the efficiency for detecting the particular final state.

The R704 and E760 experiments used similar strategies to extract the signal, evaluate the background level, and monitor the luminosity. The analysis of the center-of-mass energy distribution was improved in E760 to match the experiment goals.

3.2 *Event Detection and Analysis*

The rare events from direct formation of charmonium resonances were selected from the large background of nonresonant $\bar{p}p$ strong interactions by detecting their decays into e^+e^- or into $\gamma\gamma$, depending on the state quantum numbers. For higher $(\bar{c}c)$ excitations that do not decay directly into these two-body electromagnetic final states, one can still obtain a strong signature by detecting their inclusive decay to J/ψ or η_c, which in turn decay into e^+e^- or two photons, respectively.

The essential requirements for a detector are: *(a)* high efficiency for

events with two large transverse-momentum electrons (or photons) produced roughly back to back, which implies either a symmetric two-arm detector or a detector with full azimuthal coverage, *(b)* excellent electron/hadron and γ/π^0 discrimination and good energy and direction measurements for electrons and photons so that the mass of the decaying heavy charmonium states can be reconstructed accurately, and *(c)* hermeticity to allow complete event reconstruction. Unfortunately, in these experiments the gas-jet target apparatus blocks a considerable fraction of the backward hemisphere, thus preventing full coverage. The precision of the measurement of the final state does not influence the accuracy of the $(\bar{c}c)$ resonance measurement (which is a function

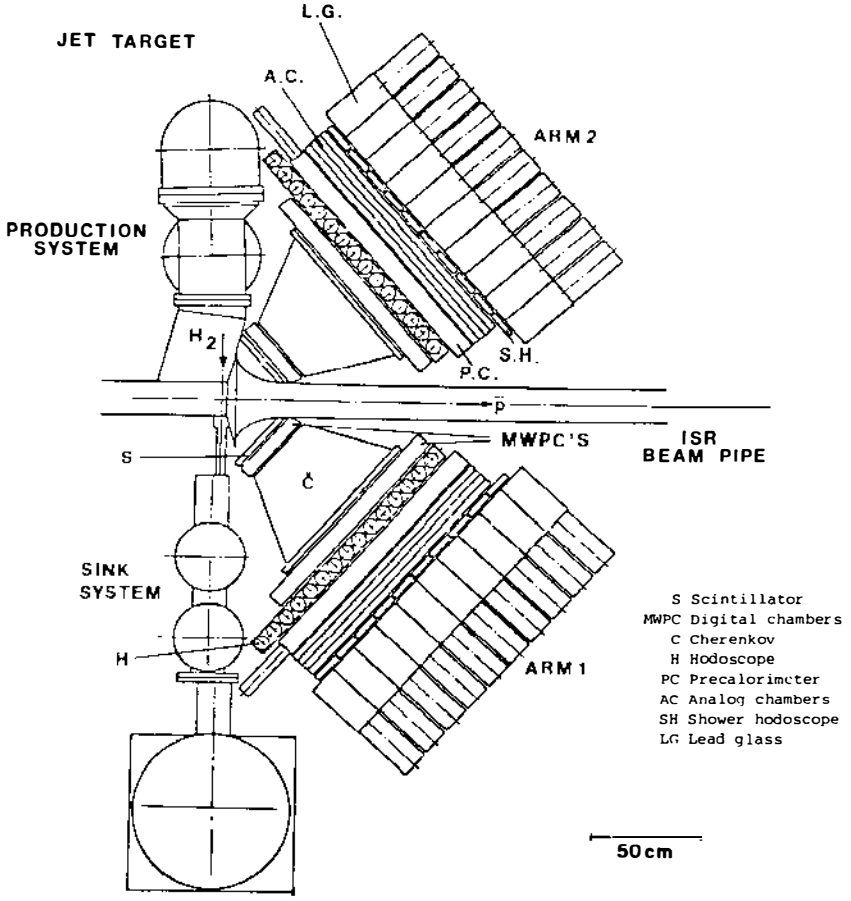

Figure 2 Top view of the R704 two-arm detector at CERN, including the target system (13).

only of the uncertainty in the energy of the beam). However, a good reconstruction of the final state is essential in suppressing the background.

Both the R704 and E760 collaborations followed these guidelines in the design of their detectors. In E760, the two-arm configuration of the R704 detector (Figure 2) was replaced by a cylindrical detector (Figure 3), thereby increasing the acceptance for events of interest by a factor of approximately five. Most of the following discussions relate to experiment E760, unless reference to experiment R704 is explicitly stated.

The selection of events with a high-mass e^+e^- in the final state was easily accomplished by identifying the electrons with the threshold gas Cherenkov counter, measuring their energy in the lead-glass central calorimeter [with $\sigma_E/E = 6\%\sqrt{E(\text{GeV})} + 1.4\%$], and determining their direction in the tracking system ($\sigma_\theta \approx 4$ mrad and $\sigma_\phi \approx 7$ mrad). The only remaining background originated from events in which two electron pairs from the Dalitz decays of π^0 or from photon conversions in the beam pipe resulted in two isolated electron tracks in the detector and a high effective mass. As an example of the results achieved, we show in Figure 4 the distribution of events as a function of the reconstructed invariant mass $m_{e^+e^-}$ for data collected at the energy of the ψ', where the average rate is approximately one event per inverse nanobarn of integrated luminosity. The large peak at the left arises from inclusive decays $\psi' \rightarrow J/\psi + X \rightarrow e^+e^- + X$, whereas the smaller peak at the higher mass results from the exclusive decay $\psi' \rightarrow e^+e^-$. The shaded area represents the residual background estimated from the events collected outside the resonance region at E_{cm}

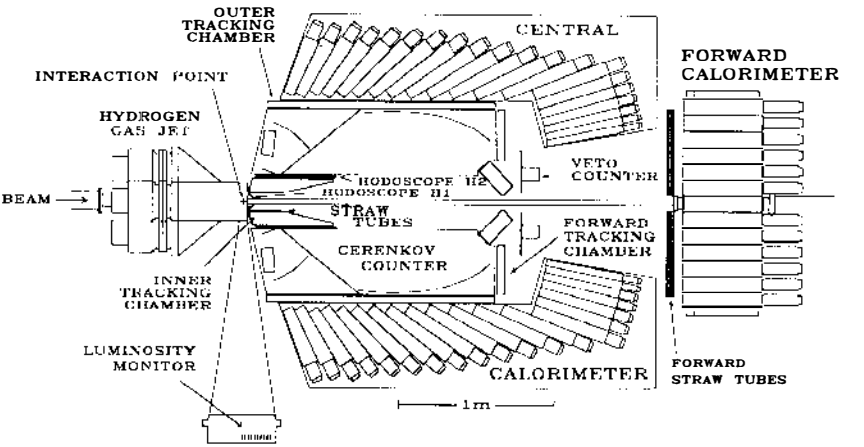

Figure 3 Layout of the E760 experiment (31) at Fermilab.

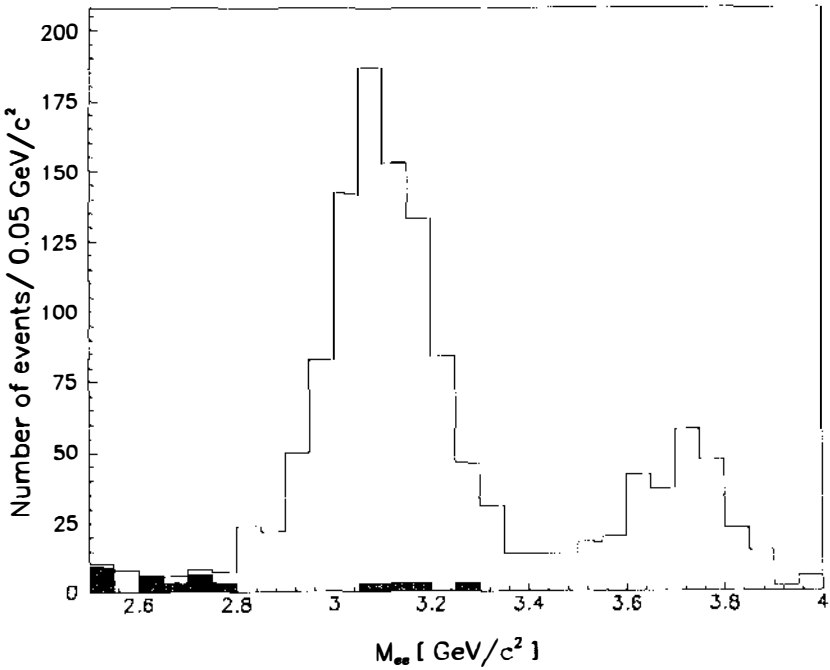

Figure 4 Invariant mass distribution of e^+e^- pairs for events recorded at the ψ' formation energy *(open area)* and off-resonance *(shaded area)*, normalized to equal luminosities (22).

The selection of events with a large-mass particle decaying to $\gamma\gamma$ was more problematic because of the large background from $\bar{p}p \rightarrow \pi^0\pi^0$ and $\bar{p}p \rightarrow \pi^0\gamma$. The worst type of background came from events in which π^0s decayed to an undetected low-energy photon and to a high-energy photon, carrying almost all of the energy of the parent π^0. To improve background rejection the search was limited to events with two or three detected photons, and in the final selection only events fitting the exclusive processes $\bar{p}p \rightarrow \gamma\gamma$ and $\bar{p}p \rightarrow \eta_c + \gamma \rightarrow \gamma\gamma + \gamma$ were retained.

3.3 *Luminosity Measurement*

The integrated luminosity for each energy setting was obtained by counting the number of recoil protons from $\bar{p}p$ elastic scattering in a silicon detector located at $\theta = 86.5°$ from the beam direction. The value of the absolute luminosity was determined (with an estimated error of ~5%) using the known $\bar{p}p$ elastic cross section, the detector acceptance, and the detector efficiency.

3.4 *Determination of the Energy Spectrum*

The beam-energy spectrum is determined from the beam-revolution frequency spectrum through the relation

$$N_{\bar{p}}G(E_{\rm cm}) = \frac{dN_{\bar{p}}}{dE_{\rm cm}} = \frac{dN_{\bar{p}}}{df}\,\eta f\,\frac{E_{\rm cm}}{\gamma\beta^2 m_p^2 c^2}. \qquad 21.$$

The factor η relates the momentum spread of the beam to the frequency spread of the beam

$$\frac{dP}{P} = \frac{1}{\eta}\frac{df}{f} \qquad 22.$$

and is defined as

$$\eta \equiv \frac{1}{\gamma^2} - \frac{1}{\gamma_t^2}. \qquad 23.$$

The transition energy factor $\gamma_t^2 \equiv (L_{\rm orb}/P)(dP/dL)$ depends on the machine's magnetic lattice.

To derive the beam energy distribution, one must determine $dN_{\bar{p}}/df$ and the η parameter of Equation 21. The frequency spectrum $dN_{\bar{p}}/df$ is determined accurately by measuring the beam-current Schottky noise. Three methods were used in E760 to estimate the value of η: *(a)* the double-scan method, *(b)* a method that relies on the measurement of the beam synchrotron frequency, and *(c)* a method that measures γ_t by changing the machine's magnetic field and using the relation $dB/B = \gamma_t^2\, df/f$. The most accurate value of η was derived from the double-scan method, which is described below; the other two methods yielded consistent results.

The measured beam-revolution frequency spectrum was well parametrized over a wide range of frequencies, with a "double Gaussian" function defined as two half-Gaussians joined at the peak. The width on the low-energy side was typically 10–20% wider than on the high-energy side. A low-energy tail caused by straggling usually contained $<0.1\%$ of the beam.

4. EXPERIMENTAL RESULTS

Most of our discussion focuses on the results from experiment E760, which recorded data for an integrated luminosity of $\sim 30\,{\rm pbarn}^{-1}$ during the summer of 1990 and the summer and fall of 1991 for a total of nine months.

In Section 4.1 we describe a set of new measurements of the param-

eters characterizing the J/ψ and ψ' resonances. These measurements provide the first determination of the natural width of these narrow states from a direct analysis of the line shape. In Section 4.2 we discuss the related measurement of the cross section for the continuum process $\bar{p}p \to e^+e^-$ in the energy range $3.0 \leq E_{cm} \leq 3.6$ GeV. This measurement led to the first determination in this energy range of the proton electromagnetic form factors in the time-like region.

Precise measurements of the $\chi_1(^3P_1)$ and $\chi_2(^3P_2)$ resonances and the discovery of the $h_c(^1P_1)$ are presented in Sections 4.3 and 4.4. We conclude this review of the experimental results with a description of *(a)* the measurements performed at the η_c and χ_2 formation energy by studying the reaction $\bar{p}p \to \gamma\gamma$ and *(b)* a search for the η_c' in the same channel.

4.1 *The* J/ψ *and the* ψ'

Figure 5 shows an example of an excitation curve obtained from the measurement of the cross section for the inclusive process $\bar{p}p \to J/\psi + \cdots \to e^+e^- + \cdots$ and for the exclusive process $\bar{p}p \to e^+e^-$ at the ψ' formation energy (22). The data are from a single store of antiprotons ($\int L(t)dt \sim 1$ pbarn^{-1}). The dashed line represents the center-of-mass energy (E_{cm}) distribution during the data taking, which had to be unfolded from the excitation curve to obtain the resonance profile. For states such as the J/ψ and ψ' in which the resonance widths are comparable to or smaller than the width of the center-of-mass energy distribution, the high level of precision obtained from the double-scan method (23) is necessary to determine the beam energy profile.

In a double scan, a resonance is scanned twice, once with the beam on the central orbit and once with the beam on a side orbit radially displaced from the central one. The frequency difference maintained between the two orbits is approximately one σ of the beam frequency spread. If the energy difference between the two orbits is known, dE/df can be readily calculated. Because the peak of the resonance defines the energy of the beam, it can be used as a marker to measure the energy difference between the two orbits.

The double-scan procedure is schematically illustrated in Figure 6. Data are first taken with the beam on the central orbit. The beam is then decelerated to the side orbit, where more data are taken. The energy and frequency of the beam change, but the B field remains the same. Finally, the beam is returned to the central orbit by changing the B field but keeping the energy constant. This procedure is repeated several times across the resonance. The resulting cross-section mea-

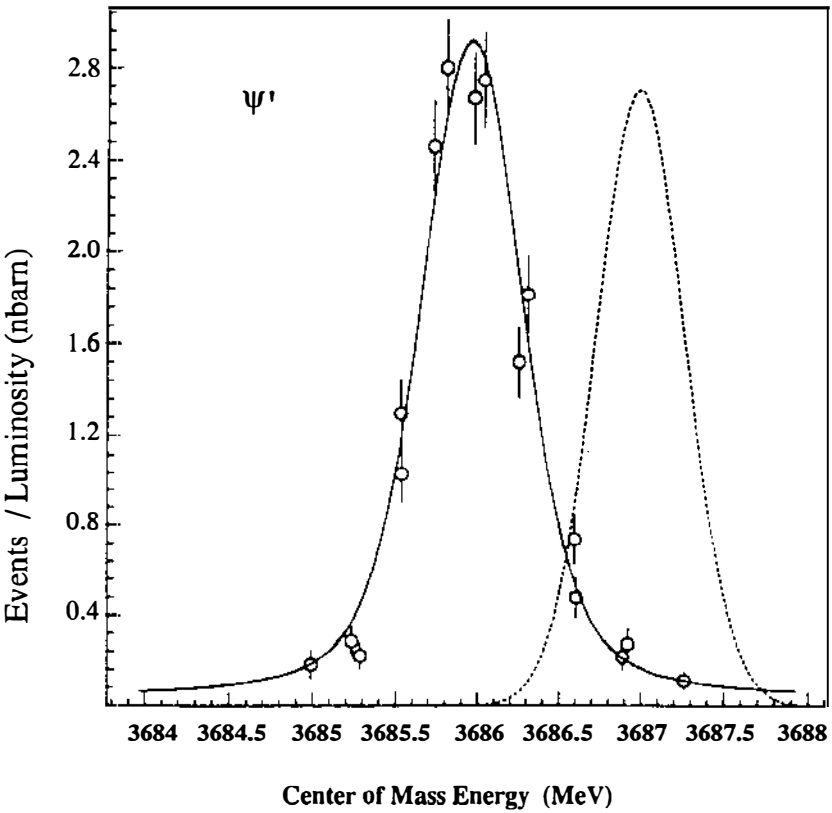

Figure 5 Events per unit luminosity for the energy scan near the ψ'. The dashed line illustrates the center-of-mass energy resolution (32).

surements can be plotted against the B field, thereby producing two excitation curves shifted with respect to each other, as shown in Figure 6.

To obtain the quantity dE/df, where E is the beam energy at constant B, one considers sets of points taken at the same magnetic field but on different orbits. The value of dE/df can be found, in essence, by forcing the excitation curve from the side orbit to match the central orbit curve. More specifically, consider the data points of Figure 6. Points 2 and 3 are taken at the same B, and points 1 and 2 are the peaks of the two excitation curves. We have

$$(E_2 - E_3) = \frac{dE}{df}(f_2 - f_3) \qquad 24.$$

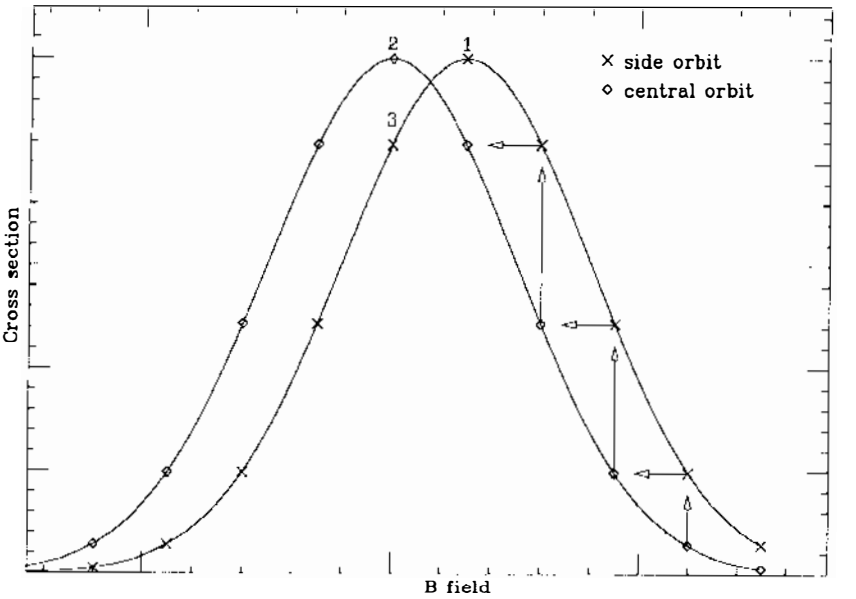

Figure 6 Schematic depicting the measurement sequence of the double scan.

and

$$(E_1 - E_3) = \beta^2\gamma^3 m_p \frac{(f_1 - f_3)}{f_3}. \qquad 25.$$

Because E_1 and E_2 are equal, Equations 24 and 25 yield

$$\frac{dE}{df} = \beta^2\gamma^3 m_p \frac{1}{f_3}\frac{(f_1 - f_3)}{(f_2 - f_3)}. \qquad 26.$$

Equivalently, η, as defined in Equation 21, is

$$\eta = \frac{1}{\gamma^2}\frac{(f_2 - f_3)}{(f_1 - f_3)}. \qquad 27.$$

We see from Equations 26 and 27 that dE/df or η can be determined accurately by this method because it depends only on frequency measurements; the parameters in the equations (β and γ) are known accurately because the resonance masses of J/ψ and ψ' are known accurately (20). Variations in orbit length for the data points on the same (central or side) orbits introduce a negligible uncertainty.

For the analysis of these narrow resonances, σ_{BW} in Equation 14 has

been modified to include the effect of radiation from the initial $\bar{p}p$ state (24). Although small, this correction decreases the measured width at the J/ψ and ψ' by ~10 and 2 keV, respectively. The resonance mass M_R is not affected. For the J/ψ, the interference between the resonant and the continuum amplitude (25) for $\bar{p}p \rightarrow e^+e^-$ is also considered but does not change the results significantly. The background for the resonance fitting procedure is determined from off-resonance data.

Figure 7 shows the results of the double-scan running for the J/ψ and ψ' from E760. From the fit to these data, the mass of the J/ψ and the total widths and product of branching ratios to $\bar{p}p$ and e^+e^- for both the J/ψ and ψ' were determined. These results are summarized in Table 2.

The mass of the J/ψ was determined by E760 to be $M_{J/\psi} = 3096.87 \pm 0.03(\text{stat.}) \pm 0.03(\text{sys.})\text{MeV}/c^2$. This value represents a small improvement over earlier measurements. To determine the branching ratios the experimenters unfolded the effects of detector efficiency and geometrical acceptance of their apparatus; this last measurement also depends on the absolute value of the luminosity.

4.2 *The Proton Electromagnetic Form Factor*

To measure the proton's electromagnetic form factor in the time-like region, the reaction $p\bar{p} \rightarrow e^+e^-$ was also studied at other energies at which no resonant production of the e^+e^- state is present. The differential cross-section for this process is given in terms of the proton magnetic and electric form factors:

$$\frac{d\sigma}{d(\cos\theta^*)} = \frac{\pi\alpha^2(\hbar c)^2}{8EP} \times \left[|G_M|^2(1 + \cos^2\theta^*) + \frac{4m_p^2}{s} |G_E|^2 \sin^2\theta^* \right], \quad 28.$$

where E and P are the center-of-mass energy and momentum of the antiproton, respectively, and θ^* is the angle between the e^- and the $\bar{p}$ in the center-of-mass system. Because the data samples used in such

Table 2 J/ψ and ψ' results from E760

	Width (KeV)	$B_{in}B_{out}$[a]	$B(pp)$[b]
J/ψ	99 ±	$(1.14^{+.16}_{-.12} \pm .10) \times 10^{-4}$	$(1.82^{+.26}_{-.19} \pm .16 \pm .06) \times 10^{-3}$
ψ'	306 ±	$(1.17^{+.14}_{-.12} \pm .08) \times 10^{-5}$	$(2.61^{+.31}_{-.27} \pm .17 \pm .17) \times 10^{-4}$

[a] $B_{in}B_{out} = B(J/\psi \rightarrow \bar{p}p)\,B(J/\psi \rightarrow e^+e^-)$ for the J/ψ, *and* $B_{in}B_{out} = B(\psi' \rightarrow \bar{p}p)\,[B(\psi' \rightarrow e^+e^-) + B(\psi' \rightarrow J/\psi X)B(J/\psi \rightarrow e^+e^-)]$ for the ψ'. The errors, in the order shown, are statistical and systematic.

[b] Using $B(J/\psi \rightarrow e^+e^-)$, $B(\psi' \rightarrow e^+e^-)$, and $B(\psi' \rightarrow J/\psi + X)$ from Ref. 20. The errors, in the order shown, are statistical, systematic, and due to the errors in the branching ratios from Ref. 20.

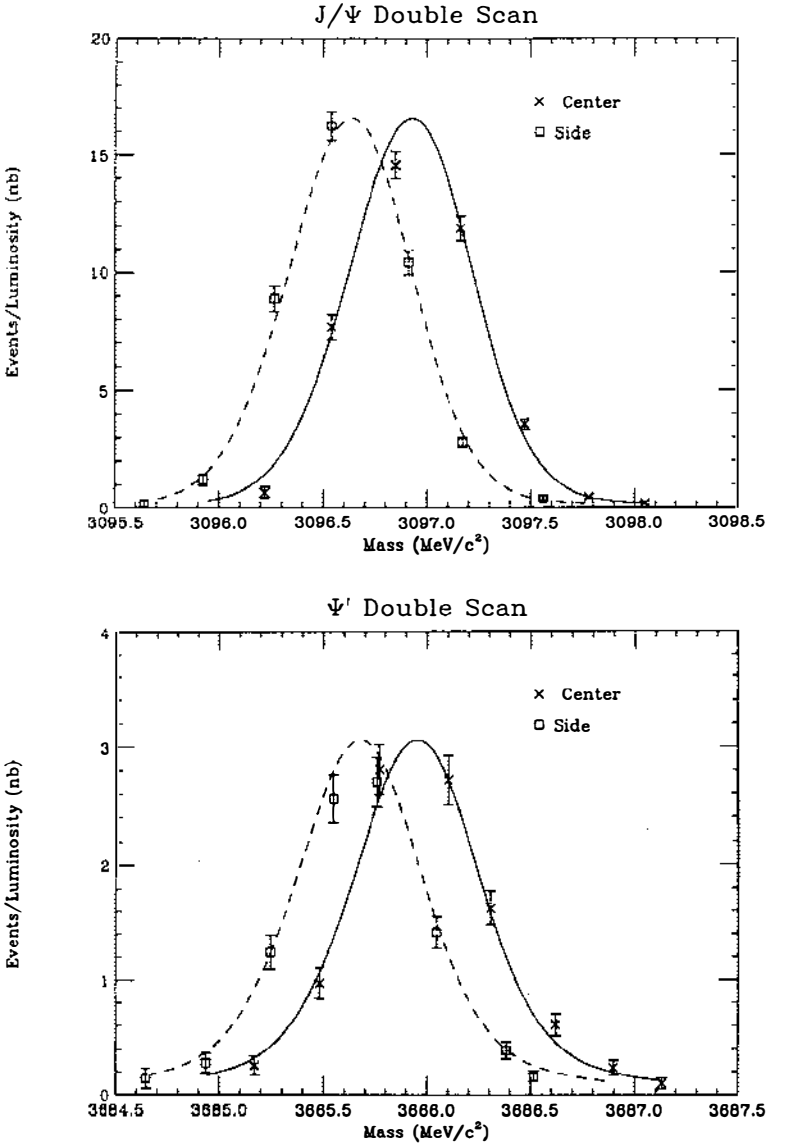

Figure 7 Data recorded during the J/ψ and ψ' double scans. The horizontal axis is the invariant mass for the central orbit. The lines are theoretical excitation curves using the best-fit parameters (22).

a study are small and cover a limited angular range, the value of $|G_M|$ is obtained under the assumption that $|G_E| = |G_M|$.

E760 has reported measurements (25) of the proton form factor at $E_{cm} = 3.0$, 3.5, and 3.6 GeV, whereas R704 was able to set only upper limits (26) in the same energy range. These results, together with measurements at lower energies, are shown in Figure 8 in the form of $q^4|G_M|/\mu_p$ vs $-q^2 = s/c^2$ ($\mu_p = 2.793$ is the magnitude of the proton's magnetic moment expressed in units of nuclear magnetons). We see that the data for $-q^2 > 5(\text{GeV/c})^2$ follow the perturbative QCD prediction (27) for large momentum transfers, i.e. $G_M(q^2) \propto q^{-4}\alpha_s^2(q^2)$, where the running strong coupling constant α_s is proportional to $1/\ln(q^2/\Lambda^2)$, with $\Lambda = 0.2$ GeV.

From the fit shown in Figure 8, one can deduce the value of the cross section for the process $\sigma(e^+e^- \rightarrow \gamma^* \rightarrow p\bar{p})$ at energies near the J/ψ and ψ' mass. From experiments carried out in e^+e^- colliders (28) one can also determine the cross-section for the similar process $\sigma(e^+e^- \rightarrow \gamma^* \rightarrow \text{hadrons})$. Thus, the branching fractions

$$f(\gamma^*) \equiv \frac{\sigma(e^+e^- \rightarrow \gamma^* \rightarrow p\bar{p})}{\sigma(e^+e^- \rightarrow \gamma^* \rightarrow \text{hadrons})} \qquad 29.$$

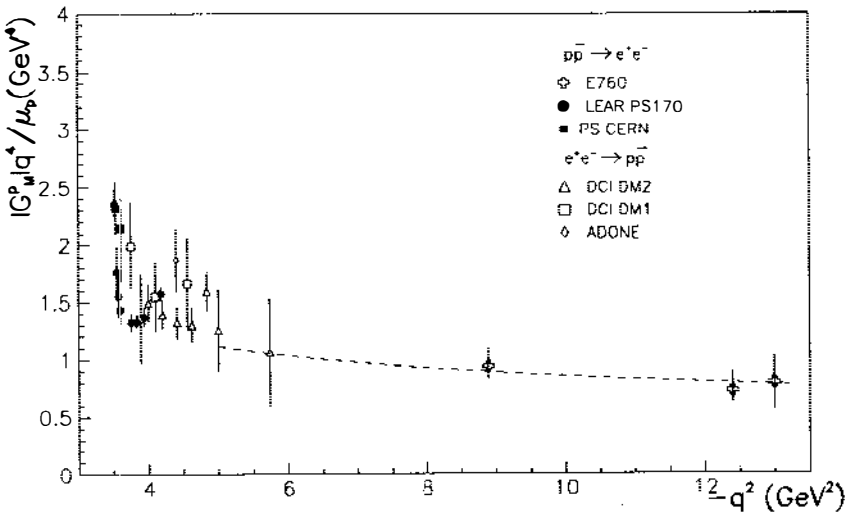

Figure 8 Variation of $q^4|G_M|/\mu_p$ with $-q^2$. The dashed curve shows a perturbative QCD fit [$q^4|G_M| \propto \alpha_s^2(q^2) \propto 1/\ln(q^2/\Lambda^2)$, with $\Lambda = 0.2$ GeV] for $-q^2 \geq 5(\text{GeV/c})^2$. From Ref. 25.

are found to be $(2.6 \pm 0.5) \times 10^{-4}$ at the J/ψ and $(0.52 \pm 0.09) \times 10^{-4}$ at the ψ'. The equivalent fractions for gluonic decays of the J/ψ and ψ', where the decay proceeds through an intermediate three-gluon state, i.e.

$$f(ggg) \equiv \frac{\Gamma(^3S_1 \rightarrow ggg \rightarrow p\bar{p})}{\Gamma(^3S_1 \rightarrow ggg \rightarrow \text{hadrons})}, \qquad 30.$$

are estimated to be $(31 \pm 2) \times 10^{-4}$ for the J/ψ, and $(12 \pm 4) \times 10^{-4}$ for the ψ'. This estimate leads to the purely experimental result that hadronization via gluons favors the $p\bar{p}$ channel by approximately one order of magnitude compared with hadronization via one photon.

4.3 The 1^3 P_J *Triplet*

The study of the production of the χ_{c1} and χ_{c2} charmonium states was conducted in a fashion similar to that used in the study of the J/ψ and

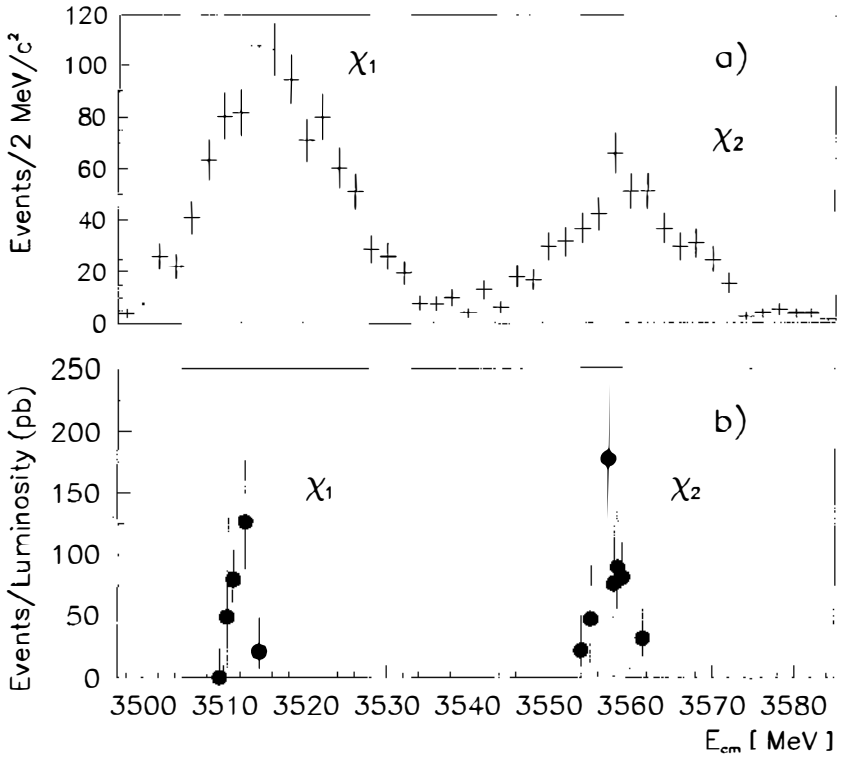

Figure 9 Comparison of the distribution of χ_{c1} and χ_{c2} events vs center-of-mass energy from *(a)* the Crystal Ball experiment (30), with *(b)* the excitation curves for χ_{c1} and χ_{c2}, measured by the R704 collaboration (29).

ψ' resonances. The reactions studied are

$$p\bar{p} \rightarrow \chi_{c1,2} \rightarrow J/\psi\,\gamma \rightarrow e^+e^-\gamma. \qquad 31.$$

Figure 9 shows the excitation curves obtained by the R704 experiment (29) as well as the mass spectra obtained by the Crystal Ball experiment at SPEAR (30). This figure graphically illustrates the advantage of the $p\bar{p}$ annihilation technique. The resolution of R704, determined only by the beam-energy resolution, is far superior to that of the Crystal Ball detector. Figure 10 depicts the excitation curves obtained by E760. As in Figure 5, the center-of-mass energy resolution is indicated as a dotted line (31, 32).

A fit to the excitation curves yields the values of the masses and total widths shown in Table 3 and, after correcting for detector efficiencies and geometrical acceptances, the values for the product $\Gamma(\chi_{c1,2} \rightarrow p\bar{p})B(\chi_{c1,2} \rightarrow J/\psi\,\gamma)B(J/\psi \rightarrow e^+e^-)$. The widths measured by E760 are more accurate than the R704 measurement because of the higher number of events (e.g. 559 events at the χ_{c2} for E760 as compared to 50 events for R704). Both masses measured by R704 are 0.8 MeV/c^2 higher than those measured by E760; this discrepancy could indicate a small

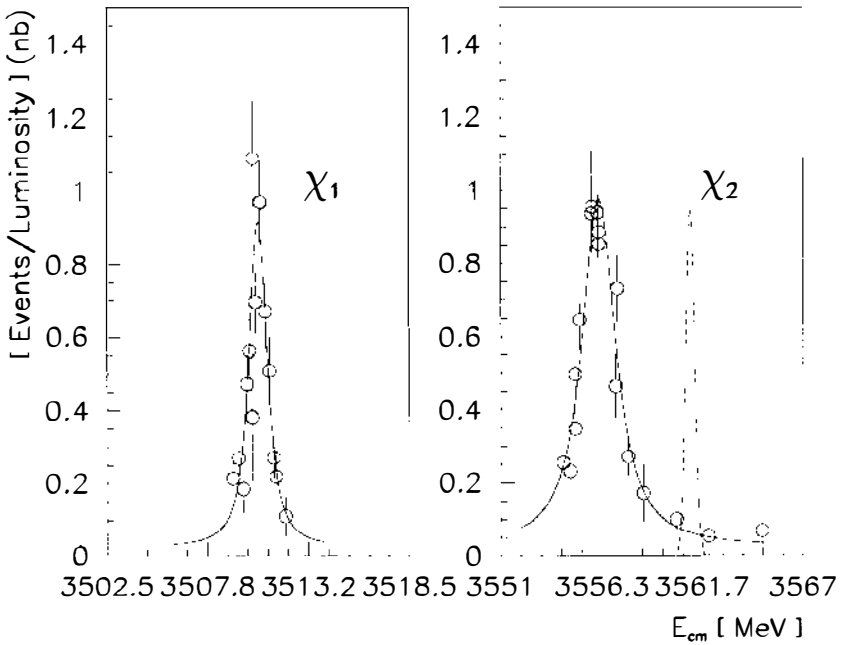

Figure 10 Excitation curves for χ_{c1} and χ_{c2} measured by the E760 collaboration (31). The dotted curve shows the resolution in the center-of-mass energy.

Table 3 χ_{c1} and χ_{c2} masses, widths, and branching ratios[a]

Parameter	R704 result	E760 result	World average[b]
$M(\chi_{c1})$ (MeV/c^2)	3511.3 ± 0.4 ± 0.4	3510.53 ± 0.04 ± 0.12	3510.53 ± 0.12
$\Gamma_{total}(\chi_{c1})$ (MeV)	<1.3	0.88 ± 0.11 ± 0.08	0.88 ± 0.14
$\Gamma(\chi_{c1} \to p\bar{p}) \times B(\chi_{c1} \to J/\psi\gamma) \times B(J/\psi \to e^+e^-)$ (eV)	$1.18^{+0.26}_{0.24}$	1.29 ± 0.09 ± 0.13	
$\Gamma(\chi_{c1} \to p\bar{p})$ (eV)			74 ± 9
$B(\chi_{c1} \to p\bar{p}) \times 10^4$			0.86 ± 0.12
$M(\chi_{c2})$ (MeV/c^2)	3556.9 ± 0.4 ± 0.5	3556.15 ± 0.07 ± 0.12	3556.17 ± 0.13
$\Gamma_{total}(\chi_{c2})$ (MeV)	$2.6^{+1.4}_{1.0}$	1.98 ± 0.17 ± 0.07	2.00 ± 0.18
$\Gamma(\chi_{c2} \to p\bar{p}) \times B(\chi_{c2} \to J/\psi\gamma) \times B(J/\psi \to e^+e^-)$ (eV)	$2.14^{+0.47}_{0.41}$	1.67 ± 0.09 ± 0.1	
$\Gamma(\chi_{c2} \to p\bar{p})$ (eV)			206 ± 22
$B(\chi_{c2} \to p\bar{p}) \times 10^4$			1.0 ± 0.1

[a] Where two errors are shown, the first is statistical and the second systematic.
[b] Using the values from Ref. 20.

difference in the absolute mass scale. E760 has used both the J/ψ and the ψ' masses as energy calibration points, thus spanning the range of the χ_c masses, whereas R704 used only the J/ψ mass for calibration.

The width of the χ_{c0} is a quantity of considerable interest because perturbative QCD calculations directly relate it to the width of the χ_{c2}. Unfortunately, the χ_{c0} has not been studied by either of the two experiments because this state does not decay readily into J/ψ [$B(\chi_{c0} \to \gamma J/\psi) = (6.6 \pm 1.8) \times 10^{-3}$] (20).

4.3.1 ANGULAR DISTRIBUTIONS IN χ_{c2} DECAYS The study of the angular distributions for the process

$$p\bar{p} \to \chi_{c2} \to J/\psi\ \gamma \to e^+e^-\ \gamma \qquad 32.$$

allows for an evaluation of the contributions of quadrupole and octupole transitions to this radiative decay. The angular distributions are described in terms of five helicity amplitudes: B_0, B_1, a_1, a_2, and a_3. Unitarity constraints allow for only three independent amplitudes. These are taken to be B_0, which describes the dynamics of χ_{c2} formation, and a_2, and a_3, which correspond to the contribution of magnetic quadrupole and electric octupole transitions in the χ_{c2} decay, respectively. a_1 characterizes the electric dipole component of the decay.

B_0 is expected to be zero in the massless QCD limit, and a_3 is expected to be zero under the hypothesis that a single quark is involved in the radiative transition. Indeed, both the E760 (33) and R704 (34) analyses yield nonzero values only for a_2, but of opposite signs. The E760 result (-0.14 ± 0.06) thus resolves the outstanding discrepancy in the sign of a_2 between the measurement of R704 ($+0.46^{+0.19}_{-0.18}$) and the value obtained from the study of $e^+e^- \rightarrow \chi_{c2} \rightarrow J/\psi\,\gamma$ by the Crystal Ball experiment (35) ($-0.33^{+0.12}_{-0.29}$). Given the value of a_2 obtained by E760, one extracts a value for the anomalous magnetic moment of the charmed quark: $\kappa_c = 0.46 \pm 0.62 \pm 0.37$, where the first error reflects the measurement uncertainties in a_2 while the second reflects theoretical uncertainties in relating a_2 to κ_c.

4.4 *The "Missing" 1^1P_1*

The singlet states of charmonium [e.g. the $\eta_c(1^1S_0, J^{PC} = 0^{-+})$, $\eta_c'(2^1S_0, J^{PC} = 0^{-+})$, and $h_c(1^1P_1, J^{PC} = 1^{+-})$] pose an unusual experimental challenge because they can be neither resonantly produced in e^+e^- annihilation ($J^{PC} = 1^{--}$) nor be produced by E1 radiative decays of the $^3S_1$ states [i.e. $J/\psi(1^3S_1, J^{PC} = 1^{--})$ and $\psi'(2^3S_1, J^{PC} = 1^{--})$]. Indeed, until quite recently only the η_c had been positively identified. One of the major objectives of the experiments studying charmonium production in $p\bar{p}$ annihilation has been to study these elusive states, and in particular to search for the h_c. The observation of this state is important not only because it is the last unidentified $n = 1$ state of charmonium but also because a comparison of its mass with the center-of-gravity mass of the three triplet ^3P states

$$m_{\text{cog}} = \frac{\sum_J (2J + 1) m_{\chi_{cJ}}}{\sum_J (2J + 1)} \qquad 33.$$

provides a measurement of the deviation of the vector part of the quark-antiquark interaction from pure one-gluon exchange. In addition, the branching ratios of the h_c hadronic decays relate to the QCD helicity selection rules, QCD multipole expansion models, and isospin conservation.

The h_c can be formed in $p\bar{p}$ through the annihilation of the initial-state particles into three gluons. It is expected to have a small width (<1 MeV) and decay with comparable rates to hadrons, and through an electric dipole transition to the $\eta_c\gamma$ final state. The cross section at the peak of the resonance for the process $p\bar{p} \rightarrow h_c$ is expected to be $<10^{-6}$ of the total cross section for $p\bar{p} \rightarrow$ hadrons.

To find the h_c, the R704 investigators searched for the inclusive decays

$$h_c \rightarrow J/\psi\, X \rightarrow e^+e^-\, X, \qquad 34.$$

while the E760 investigators searched (36) for this state by focusing on the decays

$$h_c \rightarrow \eta_c\, \gamma \rightarrow \gamma\gamma\, \gamma, \qquad 35.$$

$$h_c \rightarrow J/\psi\, \pi^0 \rightarrow e^+e^-\, \pi^0, \qquad 36.$$

and

$$h_c \rightarrow J/\psi\, 2\pi \rightarrow e^+e^-\, 2\pi. \qquad 37.$$

E760 collected data in 0.5-MeV steps near the center of gravity of the χ states. The final state for the process of Equation 35 is hard to detect because of the very small branching ratio of the decay $\eta_c \rightarrow \gamma\gamma$. No significant signal was found for this mode in E760. The other two modes

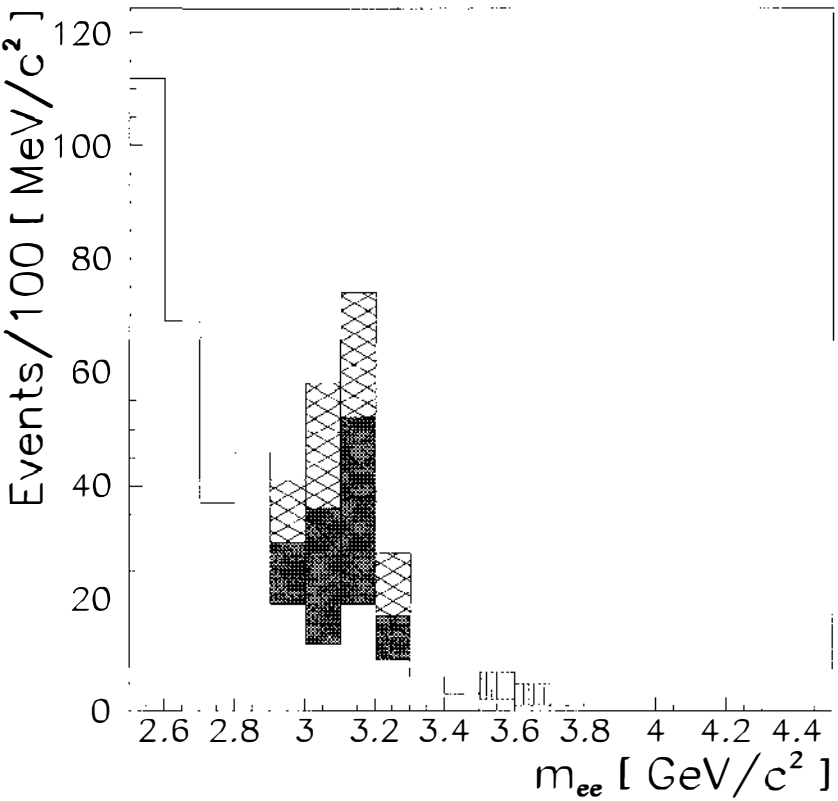

Figure 11 Invariant mass distribution of e^+e^- pairs for events collected during the 1^1P_1 search (36) of E760.

are also expected to have small branching ratios, but the J/ψ in the final state provides a very distinctive signature. Figure 11 shows the invariant mass distribution for e^+e^- pairs for all data taken during their h_c scan. A clear peak at the J/ψ mass shows that events of the type $p\bar{p} \rightarrow J/\psi\, X$ were indeed produced.

Events with $m_{e^+e^-} > 2.9$ GeV/c^2 were fitted to the reactions $p\bar{p} \rightarrow J/\psi\, \pi^0$, $p\bar{p} \rightarrow J/\psi\, 2\pi$, $p\bar{p} \rightarrow J/\psi\, \gamma$, and $p\bar{p} \rightarrow e^+e^-$ provided the event topology was compatible with the final-state hypothesis. Most of the events could be unambiguously identified as either $J/\psi\, \gamma$ (cross-hatched area in Figure 11) or $J/\psi\, \pi^0$ (solid area), although a few events were identified as $p\bar{p} \rightarrow e^+e^-$ (vertically striped area). No events were found that fit the final states $J/\psi\, \pi^0\, \pi^0$ or $J/\psi\, \pi^+\, \pi^-$. The $J/\psi\, \gamma$ events can be explained as background expected from the tails of the nearby χ_{c1} and χ_{c2} resonances.

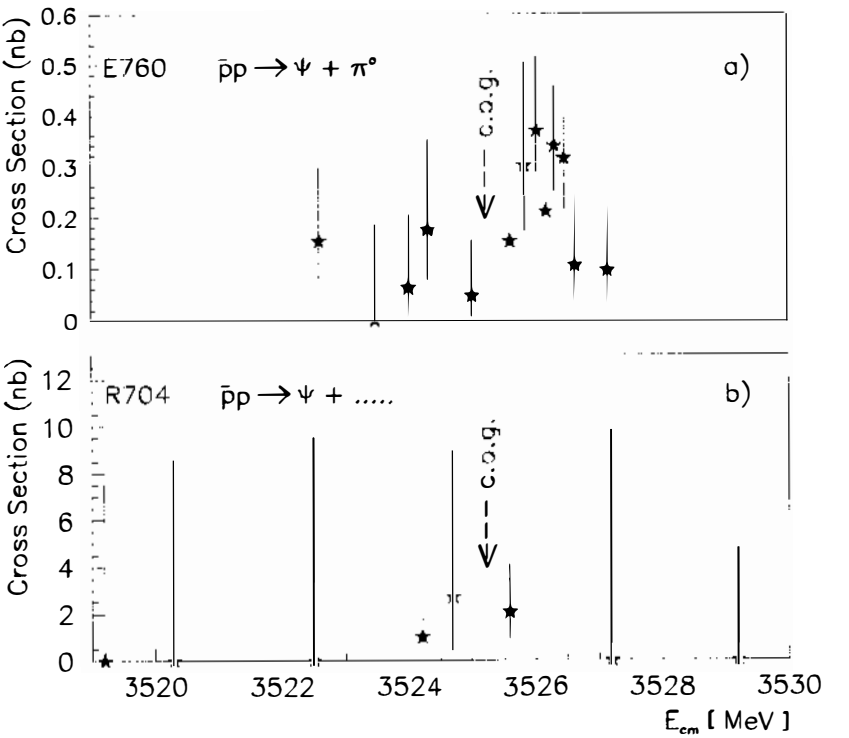

Figure 12 Cross section vs center-of-mass energy for $\bar{p}p \rightarrow \psi + \pi^0$ measured by the E760 collaboration (36), and cross section vs center-of-mass energy for $\bar{p}p \rightarrow \psi + \ldots$ measured by the R704 collaboration (37). The data are corrected for acceptance and reconstruction efficiencies to permit direct comparison.

Figure 12a shows the cross section as a function of center-of-mass energy for the reaction $p\bar{p} \rightarrow J/\psi\,\pi^0 \rightarrow (e^+e^-)\,\pi^0$. The data, binned in intervals of 150 keV in the center-of-mass energy, show for energies below $E_{\rm cog}$ a uniform level of cross section of $\sigma(p\bar{p} \rightarrow J/\psi\pi^0) = 99 \pm 40$ pbarn, which is in reasonable agreement with the prediction for this nonresonant process (38). Above $E_{\rm cog}$, an enhancement is observed near 3526 MeV that can be fitted to a resonance of mass $M = 3526.2 \pm 0.15 \pm 0.20$ MeV/c^2 and has a width compatible with the beam-energy resolution. The upper limit for the width is $\Gamma < 1.1$ MeV at 90% confidence level (c.l.)[8]. The probability that this peak is a fluctuation of the continuum is 1/400. The E760 investigators interpreted this structure to be the $h_c(1^1P_1)$ state of charmonium, a presumptive identification supported by the decay mode and by the close proximity of the mass to $M_{\rm cog} = 3525.27 \pm 0.12$ MeV.

The branching-ratio product $B(h_c \rightarrow p\bar{p})B(h_c \rightarrow J/\psi\pi^0)$ can range from $(1.7 \pm 0.4) \times 10^{-7}$ to $(2.3 \pm 0.6) \times 10^{-7}$. The lack of any candidates for the reaction $p\bar{p} \rightarrow J/\psi\,2\pi$ sets a limit to the ratio $B(h_c \rightarrow J/\psi\,2\pi)/B(h_c \rightarrow J/\psi\,\pi^0) < 0.18$ at 90% c.l.

The R704 investigators observed (37) five events consistent with process (34) at a mass of $3525.4 \pm 0.8 \pm 0.5$ MeV/c^2. They obtained a value for $\Gamma_{h_c} \times B(h_c \rightarrow p\bar{p}) \times B(h_c \rightarrow J/\psi\,X) \times B(J/\psi \rightarrow e^+e^-) = 0.135^{+0.150}_{-0.060}$ eV, while the E760 investigators determined the same quantity to be 0.010 ± 0.003 eV. The data from the two experiments are compared in Figure 12, in which the R704 data have been shifted in energy by -0.8 MeV to account for the systematic energy-scale difference between the two experiments noted in Section 4.3. The R704 events correspond to a rate 10 times higher than the cross section measured by E760 and are presumably dominated by background.

4.5 *The* $\bar{\rm p}{\rm p} \rightarrow (\bar{\rm c}{\rm c}) \rightarrow \gamma\gamma$ *Process*

Both the R704 and the E760 collaborations studied the $\eta_c(1^1S_0)$ and the $\chi_{c2}(1^3P_2)$ states via the reaction

$$\bar{p} + p \rightarrow (\bar{c}c) \rightarrow \gamma + \gamma. \qquad 38.$$

The study of this process allows the determination of $\Gamma_{\gamma\gamma} \times B(R \rightarrow p\bar{p})$ and $B(R \rightarrow \bar{p}p) \times B(R \rightarrow \gamma\gamma)$. The derived values for $B(R \rightarrow \gamma\gamma)$ and for $\Gamma_{\gamma\gamma}$, the resonance partial width into two photons, probe the physics of short-distance annihilation processes. The E760 collaboration also searched for the formation of the $\eta_c'(2^1S_0)$ resonance in the same process.

[8] Because of limited statistics, the analysis ignored the effects of possible interference between the resonance and the continuum.

4.5.1 STUDY OF THE η_c Figure 13 shows the event rate for the process $\bar{p}p \rightarrow \gamma\gamma$ as a function of the center-of-mass energy in the η_c region as measured (39) by E760. A structure is seen near 2990 MeV/c^2 above a background of comparable magnitude.

The data were fitted with the maximum likelihood method to a smooth background plus a Breit-Wigner line shape. The background cross section was adequately parametrized with a power law:

$$\sigma_{\text{back}} = A \times E_{\text{cm}}^{-B}. \qquad 39.$$

Although this background is predominantly due to misidentified $\pi^0\pi^0$

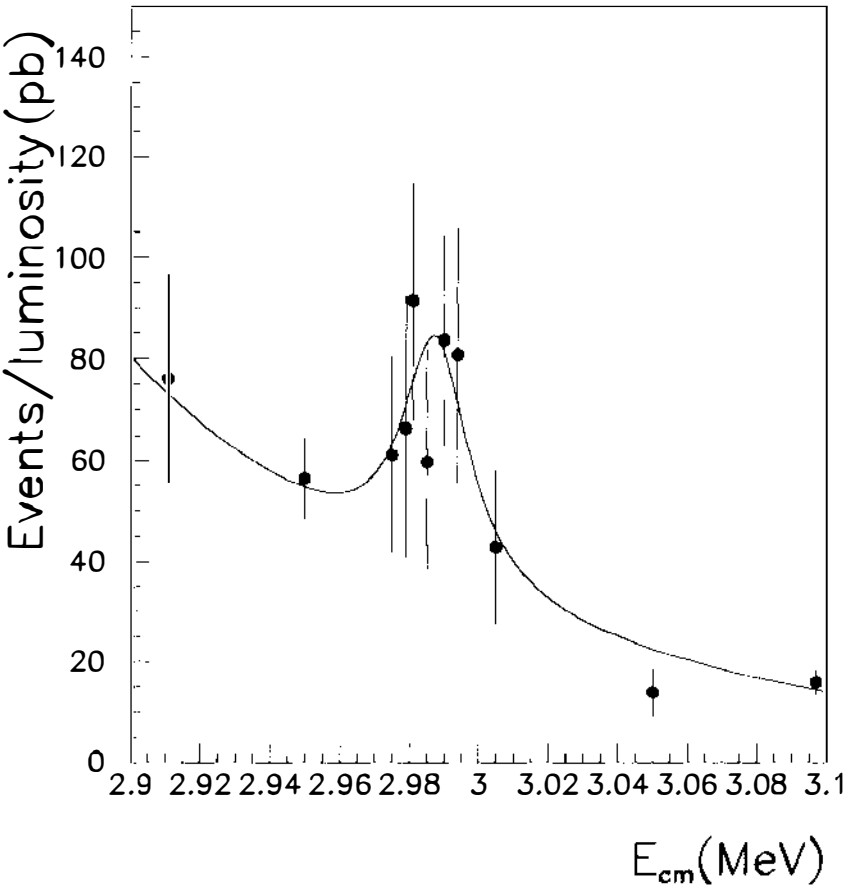

Figure 13 Measured (39) event rate for $\bar{p}p \rightarrow \gamma\gamma$ vs center-of-mass energy at η_c. To optimize the signal to background ratio the events were selected with $|\cos(\theta^*_\gamma)| \leq 0.25$ for the $\gamma\bar{p}$ angle in the center-of-mass system.

and $\pi^0\gamma$ events, the presence of a small component of genuine nonresonant $\bar{p}p \rightarrow \gamma\gamma$ events cannot be ruled out. The analysis of the data assumes complete incoherence between signal and background and thus could yield misleading results in the presence of interference effects between the amplitude for resonant production and the amplitude for the nonresonant continuum. Unfortunately, the data sample is too small to allow for a more global analysis.

The values for M_{η_c} obtained by E760 and R704 (40) are $2987.5^{+3.0}_{-2.8}$ MeV/c^2 and $2982.6^{+2.7}_{-2.3}$ MeV/c^2, respectively. One can compare these values with the world average (20) of 2978.8 ± 1.9 MeV/c^2. In Table 4 we compare values for $\Gamma_{\gamma\gamma}$, $B(\eta_c \rightarrow \bar{p}p)$ and $B(\eta_c \rightarrow \gamma\gamma) \times B(\eta_c \rightarrow \bar{p}p)$ from E760 (preliminary values) and R704 with results from other recent experiments and with theoretical predictions.

4.5.2 MEASUREMENT OF THE DECAY RATE FOR $\chi_2 \rightarrow \gamma\gamma$ AND A SEARCH FOR THE η_c' Figure 14 shows the yield of $\bar{p}p \rightarrow \gamma\gamma$ events collected (39, 50) by the E760 collaboration in the range $3520 \leq E_{cm} \leq 3690$ MeV, where 1P and 2S charmonium resonances are formed. A 4σ excess over background is evident at 3556 MeV, the mass of the χ_{c2}. This excess of events, fitted with a Breit-Wigner distribution for the χ_{c2} mass and width, gives for the product of branching ratios $B(\chi_2 \rightarrow \bar{p}p) \times B(\chi_2 \rightarrow$

Table 4 *η_c widths and branching ratios*

	$B(\eta_c \rightarrow \gamma\gamma) \times B(\eta_c \rightarrow \bar{p}p)$ in units of 10^{-8}	$B(\eta_c \rightarrow \gamma\gamma)$ in units of 10^{-4}	$\Gamma(\eta_c \rightarrow \gamma\gamma)$ (keV)
Experiment			
E760 (39)	35.4 ± 7.6	3.0 ± 0.7 ± 1.0[a]	$7.0^{+2.9}_{-2.0}$ ± 2.3[a]
R704 (40)	68^{+42}_{-31}		
CLEO (41)			5.7 ± 1.8 ± 1.6
TPC (42)			$6.4^{+5.0}_{-3.4}$
PLUTO (43)			33^{+15}_{-12} ± 9[b]
TASSO (44)			19.9 ± 6.1 ± 8.6
ARGUS (45)			12.2 ± 3.0
L3 (46)			8.0 ± 2.3 ± 2.4
Theory			
PQCD (47)[c]		$3.1^{+0.5}_{-0.4}$	
B.A. (48, 49)			3–5

[a] Using the Particle Data Group (20) value $B(\eta_c \rightarrow \bar{p}p) = (12 \pm 4) \times 10^{-4}$. The first errors quoted come from the E760 measurement, whereas the second ones reflect the uncertainties in the values taken from other experiments.

[b] Value calculated from the PLUTO measurement of $B(\eta_c \rightarrow K_S K^{\pm}\pi^{\mp}) \times B(\eta_c \rightarrow \gamma\gamma)$, using the Particle Data Group (20) value $B(\eta_c \rightarrow K\bar{K}\pi) = (6.6 \pm 1.8) \times 10^{-2}$. The first error quoted comes from the PLUTO measurement, whereas the second one reflect the uncertainties in $B(\eta_c \rightarrow K\bar{K}\pi)$

[c] Using the value $\alpha_s(m_c) = 0.276 \pm 0.014$ (47). The error quoted is due only to the uncertainty in the value of α_s.

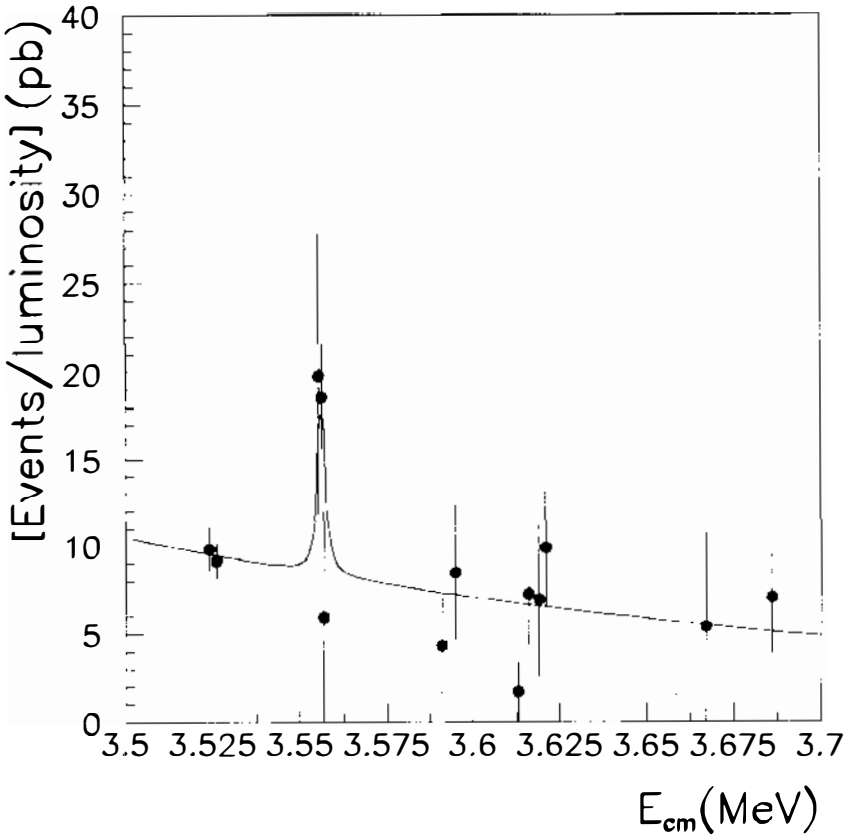

Figure 14 Measured (39, 50) event rate for $\bar{p}p \rightarrow \gamma\gamma$ vs center-of-mass energy near the $1P$ and $2S$ states. These events were selected cutting at $|\cos(\theta^*_\gamma)| \leq 0.4$.

$\gamma\gamma) = (1.60 \pm 0.39 \pm 0.16) \times 10^{-8}$. Using the values of $\Gamma_{\chi 2}$ and $B(\chi_2 \rightarrow \bar{p}p)$ from the same experiment, one derives the values of $B(\chi_2 \rightarrow \gamma\gamma)$ and of the partial decay width to $\gamma\gamma$. These values are compared with results from e^+e^- experiments in Table 5, which also includes the results obtained by R704 (40).

The energy range spanned by these data overlaps the mass region where the η_c' was observed in the Crystal Ball experiment (55). The lack of any enhancement in that region is taken as an indication that a more systematic and higher sensitivity search for the η_c' must be performed. In this respect we can look with some optimism to the future data from the E835 experiment, a continuation of E760.

Table 5 $\chi_{c2} \rightarrow \gamma\gamma$ width and branching ratio

	$\Gamma(\chi_{c2} \rightarrow \gamma\gamma)$(keV)	$B(\chi_{c2} \rightarrow \gamma\gamma)(10^{-4})$
Experiment		
E760 (50)	$0.32 \pm 0.08 \pm 0.05$	$1.6 \pm 0.4 \pm 0.2$
R704 (40)	$2.9^{+1.3}_{-1.0} \pm 1.7^{a}$	$11^{+5}_{-4} \pm 4^{a}$
CLEO (41)	<1.0 (95% c.l.)	
VENUS (51)	<4.2 (95% c.l.)	
TPC (42)	<4.2 (95% c.l.)	
Crystal Ball (52)	2.8 ± 2.0	
DASP (20, 53)	<1.6 (90% c.l.)	
Theory		
PQCD (47)	0.81 ± 0.15^{b}	
B.A. (49)	0.56	
B.B.L. (54)		4.1 ± 1.1 ($\pm 36\%$)

[a] Assuming isotropic angular distribution and $\Gamma(\chi_{c2}) = 2.6^{+1.8}_{-1.0}$ MeV.
[b] Using $\Gamma(\chi_{c2} \rightarrow gg) = 1.71 \pm 0.21$ MeV and $\alpha_s = 0.276 \pm 0.014$.

5. INTERPRETATION OF THE EXPERIMENTAL RESULTS

Precise measurements of the quarkonium states can in principle lead to the determination of the fundamental parameters of QCD, the mass of the constituent quarks, and the coupling constant of strong interactions, just as the study of positronium and of the hydrogen atom are sufficient to derive the mass of the electron and the fine-structure coupling constant.

In this section we first briefly review some aspects of charmonium phenomenology (Sections 5.1 and 5.2) and then discuss in Section 5.3 attempts to derive the parameters of the theory from the experimental results presented in this review.

5.1 *Charmonium Dynamics*

Charmonium, the bound system of a charmed quark and its antiquark, should in principle be completely described within the framework of QCD. Although such a description has not yet been achieved, significant progress has been made in two approaches: one through lattice QCD calculations and the other through potential models.

Lattice calculations (6) start from the Lagrangian of QCD and attempt to solve the equations of motion numerically on a discrete lattice of space-time points and to extract physically meaningful quantities by taking the appropriate limits (small lattice spacing and large lattice volume). In principle this approach should be exact, but in practice lattice QCD calculations still make simplifying assumptions and do not yet

completely describe charmonium. Nevertheless, certain quantities, e.g. the level spacing between the $1P$ and $1S$ states as a function of the strong coupling constant, can be reliably calculated using this technique (56). This calculation has been used to determine the value of the strong coupling constant from the observed level spacing. From the mass measurements for the η_c, J/ψ, h_c and the χ_cs from the $p\bar{p}$ and e^+e^- experiments, one obtains the value of $\alpha_{\overline{MS}}(5\text{ GeV}) = 0.174 \pm 0.012$. Equivalently, $\Lambda^{(4)}_{\overline{MS}} = 160^{+47}_{-37}$ MeV or, by extrapolating to the mass of the Z, $\alpha_{\overline{MS}}(M_Z) = 0.105 \pm 0.004$, a value comparable in accuracy to that obtained in high-energy e^+e^- experiments.

In the potential model approach (5, 57), a phenomenological potential $V(r)$ is used to describe the interaction between the c and $\bar{c}$ quarks. Because the radius of the system ($r_B = (\frac{2}{3}\alpha_s m_c)^{-1} \approx 1$ fermi) is large, the effects of strong long-range binding forces must be included, i.e. the interaction must become strong at large separation. The funnel potential $V(r) = a/r + kr$ provides a simple example of a QCD-inspired potential. The Coulomb-like term describes the short-distance behavior expected for one-gluon exchange, with $a = -\frac{4}{3}\alpha_s(r)$ proportional to the running coupling constant. The constant $k \approx 0.15$ GeV^2 in the confining term measures the string tension. Other functional forms for the potential have been used in the literature; the spin-averaged level structure is quite insensitive to the form used, provided some general conditions are satisfied that are required for the correct ordering of the levels, i.e. $\nabla^2 V(r) > 0$ and $(d/dr)(1/r)[dV(r)/dr] < 0$ (58).

The potential $V(r)$ may include terms arising from the most general spin structure of the quark-antiquark interaction (scalar, vector, axial vector, pseudoscalar, and tensor), but the existence of pseudoscalar and of vector charmonium states implies that the dominant terms are due to vector and scalar exchange. Perturbation theory shows that the short-distance part of the potential is dominated by single-gluon—and thus vector—exchange, whereas the level spacing of the χ_c states and results from lattice QCD (59) suggest that the long-range confining potential is predominantly the result of an effective scalar exchange.

Starting from a central potential $V(r)$, one derives[9] the Breit-Fermi Hamiltonian of a system of two interacting fermions of equal mass containing relativistic corrections up to order v^2/c^2. This approximation is acceptable because in the $(c\bar{c})$ system typical velocities for the two quarks are $v/c \sim 0.5$. The Breit-Fermi Hamiltonian is

[9] The Breit-Fermi Hamiltonian was derived from the static nonrelativistic reduction (60) of the Bethe-Salpeter equation with relativistic corrections to order $1/m^2$, or from the Wilson loop technique (61).

$$H = H_0 + H_1$$
$$= [2m + p^2/m - p^4/(4m^3) + V(r)] + (H_{SI} + H_{LS} + H_T + H_{SS}), \quad 40.$$

where the term H_1 (with $H_1 \ll H_0$) includes, in addition to the spin-independent part H_{SI}, terms that describe the spin-orbit interaction

$$H_{LS} = \mathbf{L}\cdot(\mathbf{S}_1 + \mathbf{S}_2)\frac{1}{2m^2r}(3V_v' - V_s'), \quad 41.$$

the tensor interaction

$$H_T = [(\mathbf{S}_1\cdot\hat{\mathbf{r}})(\mathbf{S}_2\cdot\hat{\mathbf{r}}) - (\mathbf{S}_1\cdot\mathbf{S}_2)/3]\frac{1}{m^2r}(V_v' - rV_v''), \quad 42.$$

and the spin-spin interaction

$$H_{SS} = (\mathbf{S}_1\cdot\mathbf{S}_2)\frac{2}{3m^2}\nabla^2 V_v. \quad 43.$$

Here $\mathbf{L}$, $\mathbf{S}_1$, and $\mathbf{S}_2$ are the orbital and spin-angular momenta; V_v and V_s (with $V = V_v + V_s$) transform as the time component of a four vector and as a Lorentz scalar, respectively; m is the quark mass; and primed quantities stand for the derivative d/dr.

The hyperfine splittings

$$\Delta E_S = M(^3S_1) - M(^1S_0) \quad 44.$$

and

$$\Delta E_P = M_{cog}(^3P) - M(^1P_1) \quad 45.$$

are completely determined by the H_{SS} term.[10] Under the hypothesis that the vector part of the interaction is dominated by single-gluon exchange, the hyperfine splitting reduces to

$$\Delta E_{S,P} \propto \langle \nabla^2 V_v(r) \rangle - \left\langle -\frac{4\alpha_s}{3}\nabla^2\left(\frac{1}{r}\right)\right\rangle = \frac{-4\alpha_s}{3} \times |\psi(0)|^2, \quad 46.$$

where the expectation value is evaluated using the unperturbed wavefunction $\psi(r)$. Since $\Delta E_{S,P}$ is proportional to the square of the wavefunction at the origin, then for single-gluon exchange, $L \neq 0$ singlet states would be degenerate with the triplet center-of-gravity. Therefore, the observation of such a hyperfine splitting signals deviations from the simple single-gluon exchange hypothesis.

[10] The quantity $M_{cog}(^3P)$ in Equation 45 was defined in Section 4.4.

5.2 *Charmonium Decay Rates*

Decays of charmonium states that proceed through the annihilation of the quark-antiquark pair into e^+e^-, $\gamma\gamma$, or multigluon final states can be factored into two parts: one that gives the probability of finding the quark-antiquark pair at a distance at which the annihilation can take place (~Compton wavelength of the quark $\lambda_Q = 1/m$) and one describing the on-shell $c\bar{c}$ hard process. The first factor can be expressed in terms of the wavefunctions for the $c\bar{c}$ system, while the second factor is evaluated using perturbative QCD.

In the Born approximation, a nonrelativistic derivation of the width for the decay of a singlet S state of mass M to $\gamma\gamma$ gives

$$\Gamma(^1S_0 \to \gamma\gamma) = \frac{48\pi e_c^4 \alpha^2}{M^2} |\psi(0)|^2 \left(1 - \frac{3.4\alpha_s}{\pi}\right), \qquad 47.$$

where $e_c = 2/3$ is the c-quark charge in electron charge units and α is the fine structure constant. The last factor includes first-order strong radiative corrections (47).

A generalization to hadronic processes such as

$$^1S_0, {}^3P_0, \text{ or } {}^3P_2 \to gg; \; {}^3S_1 \text{ or } {}^1P_1 \to ggg; \; {}^3P_1 \to gq\bar{q}, \qquad 48.$$

where the final-state constituents fragment into light hadrons, gives for a state of principal quantum number n and orbital angular momentum l the decay width

$$\Gamma[(\bar{c}c)_{nl} \to \text{light hadrons}] \propto \left|\frac{d^l}{dr^l}\psi_{nl}(0)\right|^2 F(\alpha_s), \qquad 49.$$

where $F(\alpha_s)$ is a power series in α_s. For P states, calculations along these lines lead to infrared divergences at order α_s^3, i.e. to leading order for $^3P_1$ and $^1P_1$ states and to next-to-leading order for $^3P_2$ and $^3P_0$ states. In a recent paper Bodwin et al (54) point out that the appearance of infrared divergences is an indication of the breakdown of the adopted factorization scheme and suggest an alternate factorization scheme.

The hadronization process by which gluons transform into light-quark hadrons is not well understood. For hadronization into a proton-antiproton pair, which also determines the cross section for $(\bar{c}c)$ formation in the reaction $\bar{p}p \to (\bar{c}c)$, estimates of the coupling of $(\bar{c}c)$ states to $\bar{p}p$ have been obtained in the framework of massless QCD (62). The vector coupling of QCD requires that massless quarks have opposite helicities, a requirement that carries over to the annihilating p and $\bar{p}$. Thus only states of helicity ± 1 can be formed, and the formation of

$J = 0$ states, such as the η_c and the χ_{c0}, is forbidden. This rule is badly violated, which is not surprising since, in this energy regime, the mass of the proton is hardly a negligible quantity. An alternate model describes baryons as compound objects of quarks and diquark structures (63), but this model predicts for the partial width for $\eta_c \rightarrow p\bar{p}$ a value much smaller than the one measured.

Radiative (64) or gluonic (65) transitions between two states of charmonium can be expressed in terms of multipoles of the electromagnetic or gluonic field.

For P to S radiative decays

$$(\bar{c}c)_{n,l} \rightarrow (\bar{c}c)_{n',l'} + \gamma, \qquad 50.$$

where $n' = n$ and $l' = l \pm 1$, the electric-dipole term dominates. In the limit of large wavelengths we have

$$\Gamma_{fi} = \frac{4}{9} e_c^2 \alpha k^3 |\langle f|\mathbf{r}|i\rangle|^2, \qquad 51.$$

where $k = E_i - E_f$, the differences between the energies of the initial and final state, and $\mathbf{r} = \mathbf{r}_1 - \mathbf{r}_2$. For charmonium, the long wavelength limit ($kr_B \ll 1$) is not satisfied, and corrections of order of 10% must be applied for P to S transitions of states with equal n. The value of the overlap integral is sensitive to the choice of the potential used to derive the wavefunctions for the initial and final states, and relativistic corrections can be substantial. For example, in the decay $1^1P_1 \rightarrow 1^1S_0 + \gamma$, spin effects tend to shrink the wavefunction of the $^1S_0$, thereby reducing the overlap with the $^1P_1$ state. Experimental values for $\Gamma(\chi_{c0,1,2} \rightarrow \psi + \gamma)$ are in good agreement with predictions of recent calculations that include such relativistic corrections (54, 66, 67). The same authors predict $\Gamma(1^1P_1 \rightarrow \eta_c + \gamma) \approx 400$ keV.

The evaluation of transition rates for processes that involve the emission of light quarks from the charmonium states, e.g.[11]

$$(c\bar{c}) \rightarrow (c\bar{c})' + \pi^0; \; (c\bar{c}) \rightarrow (c\bar{c})' + \pi\pi, \qquad 52.$$

is more complicated. Perturbative QCD is not applicable in this case, in which we have small energy difference and soft gluon emission, and one must resort to phenomenological models. Two conflicting predictions (68, 69) have been made for the relative decay rates of the $^1P_1$ to $\psi\pi^0$ and to $\psi\pi\pi$; the results of E760 will help clarify this discrepancy.

5.3 *Determination of* α_s *from Charmonium Data*

5.3.1 ANNIHILATIONS The rate of charmonium decays via annihilation depend on the charmed quark mass m, the wavefunction of the

[11] The first decay mode shown does not conserve isospin.

system at the origin $\psi(0)$, and the strong coupling constant α_s. Ratios of rates for two annihilation processes of the same state are largely independent of m and $\psi(0)$. In principle, one should be able to extract from such ratios a value for α_s. However, only calculations to next-to-leading order in the perturbation series are available. These yield results that are not unique but that depend on the precise definition of the coupling constant (the renormalization scheme) and on the choice of the mass μ (the renormalization scale) at which α_s is defined.[12] These unphysical ambiguities will disappear in calculations made to all orders. For some processes the next-to-leading order term is comparable in magnitude to the leading-order term, and the convergence of the perturbation series is in question. Without discussing this treacherous subject further, we compare the quoted experimental results to the expressions given in Equation 47 in which $\mu = m = 1.5$ GeV is chosen.[13] For the η_c,

$$\frac{\Gamma(\eta_c \to \gamma\gamma)}{\Gamma(\eta_c \to \text{gluons})} = \frac{8\alpha^2}{9\alpha_s^2} \frac{1 - 3.4\alpha_s/\pi}{1 + 4.8\alpha_s/\pi} \sim B(\eta_c \to \gamma\gamma) = (3.0 \pm 1.2) \times 10^{-4}, \quad 53.$$

from which $\alpha_s(\mu = 1.5 \text{ GeV}) = 0.40^{+0.11}_{-0.07}$ to leading order or $\alpha_s(\mu = 1.5 \text{ GeV}) = 0.28^{+0.06}_{-0.04}$ to next-to-leading order.

One is tempted to apply the same method to extract α_s from the ratio

$$\frac{\Gamma(\chi_{c2} \to \gamma\gamma)}{\Gamma(\chi_{c2} \to \text{gluons})} = (1.9 \pm 0.6) \times 10^{-4} \quad 54.$$

to obtain $\alpha_s(\mu = 1.5 \text{ GeV}) = 0.50^{+.10}_{-.07}$ to leading order and $\alpha_s(\mu = 1.5 \text{ GeV}) = 0.36 \pm 0.04$ to next-to-leading order. However, as we have seen, the presence of infrared divergences in the next-to-leading order corrections casts doubt on the validity of this derivation.

5.3.2 THE HYPERFINE SPLITTINGS The values for the hyperfine splitting are

$$\Delta E_S = M(J/\psi) - M(\eta_c) = 109.4^{+3.0}_{-2.8} \text{ MeV} \quad 55.$$

and

$$\Delta E_P = M_{\text{cog}} - M(h_c) = -0.93 \pm 0.28 \text{ MeV}, \quad 56.$$

[12] The literature contains suggestions for how to choose the renormalization scale in a way that minimizes these ambiguities (70).

[13] Note that the α_s used in the discussion of this section is the one defined in the modified minimal subtraction scheme, i.e. $\alpha_{\overline{MS}}$.

where we have used the masses for the J/ψ, η_c, χ_{c1}, χ_{c2}, and h_c obtained by E760 and the χ_{c0} mass of 3415.1 ± 1.0 MeV (20). This choice yields M_{cog} = 3525.27 ± 0.12 MeV.

The fact that ΔE_P is negative excludes many of the mechanisms proposed to shift the h_c mass from M_{cog} (72).[14] The correct sign and magnitude for this shift is predicted by an approach (73) that evaluates the hyperfine splitting to one loop in perturbative QCD. In a recent version of this calculation (74) ΔE_P does not depend on the mass scale (μ) and the renormalization scheme but only on the value of the coupling constant α_s and of the mass of the constituent quark m. From the measured value of ΔE_P one finds that α_s = 0.28 ± .02 for m = 1.2 GeV or α_s = 0.33 ± .02 for m = 1.8 GeV. In contrast, the hyperfine splitting of the S states as given in Ref. 74 is not independent of the renormalization scale. For the choice $\mu = m$, one finds from the comparison with the experimental result values of α_s vs m consistent with the result obtained for the P states. With this choice for the mass scale, the contribution of the second-order corrections is much smaller than that of the leading order, as one would expcct for a reliable application of perturbative QCD.

5.3.3 CONCLUSIONS The derivation of α_s from charmonium data presents several problems. If one uses the ratio of the measured annihilation rates of the η_c into $\gamma\gamma$ and light hadrons, one has to deal with large uncertainties in the measured value of $B(\eta_c \rightarrow \gamma\gamma)$ and, more importantly, one is limited by the poor understanding of the convergence of the perturbation series and of the ambiguities introduced by thc choice of a mass scale. The estimation of α_s from the hyperfine splitting of P states is more robust because it is based on a more precise measurement and is less affected by such theoretical uncertainties. However, the value derived for α_s in this manner still depends on the value of the mass of the constituent quark, a quantity that is rather poorly defined.

The determination of α_s using the $1S - 1P$ mass splitting as an input to lattice gauge calculations is one of the most reliable methods at present. As the methods used in these calculations improve, this technique will probably yield the best measurement for α_s. The value of α_s(5 GeV) = 0.174 ± 0.012 of Ref. 56 extrapolated to our energy scale gives $\alpha_s(1.2\ \text{GeV}) = 0.279^{+0.038}_{-0.028}$ and $\alpha_s(1.5\ \text{GeV}) = 0.253^{+0.032}_{-0.022}$.

[14] See Ref. 72 for earlier references on evaluations of ΔE_P.

6. OUTLOOK

It has been 20 years since the discovery of charmonium swept the field of particle physics, and still the study of this system remains a vital and worthwhile endeavor. The high precision measurements achieved through the study of charmonium produced in proton-antiproton annihilations and the opportunity to discover states not accessible in electron-positron annihilations are the major reasons for the vitality of such experiments. It is surprising to note that with the observation of the $h_c(1^1P_1)$, our qualitative knowledge of the charmonium spectrum is now more complete than our knowledge of the positronium spectrum!

Just as positronium has been one of the proving grounds of quantum electrodynamics charmonium has provided some of the more stringent tests of QCD. The new precise measurements from R704 and E760 make comparisons with theory even more challenging. We look forward to the continuation of this series of experiments at Fermilab (75), where more accurate measurements of the χ_{c0}, h_c, η_c, η_c' states as well as the potential to observe as yet undetected states of charmonium (such as the $^3D_2$, $^1D_2$) will extend the range of tests of QCD.

Literature Cited

1. Gross D, Wilczek F. *Phys. Rev. Lett.* 30:1343 (1973); Politzer HD. *Phys. Rev. Lett.* 30:1346 (1973)
2. Aubert JJ, et al. *Phys. Rev. Lett.* 33: 1404 (1974); Augustin JE, et al. *Phys. Rev. Lett.* 33:1406 (1974)
3. Feldman GJ, Perl ML. *Phys. Rep.* C19:233 (1975); Feldman GJ, Perl ML. *Phys. Rep.* C33:285 (1977)
4. Eichten E, et al. *Phys. Rev. Lett.* 34: 369 (1975)
5. *Quarkonia, Current Physics—Sources and Comments; Vol. 9*, ed. W Buchmüler. Amsterdam: North-Holland (1992)
6. Kronfeld AS, Mackenzie PB. *Annu. Rev. Nucl. Part. Sci.* 43:793 (1993); Mackenzie PB. 1993. In *Lattice 92, Int. Symp. Lattice Field Theory*, ed. J Smit, P Van Baal. *Nucl. Phys.* B30(Proc. Suppl.):35 (1993); Lepage GP. In *Lattice 91, Int. Symp. Lattice Field Theory*, ed. M Fukugita, et al. *Nucl. Phys.* B26(Proc. Suppl.):45 (1992)
7. Fitch VL, private communication. See also Ref. 18 in our Ref. 4.
8. Cole FT, Mills FE. *Annu. Rev. Nucl. Part. Sci.* 31:295 (1981); Möhl D, et al. *Phys. Rep.* C58:73 (1980)
9. Arnison G, et al. *Phys. Lett.* B122:103 (1983); Arnison G, et al. *Phys. Lett.* B126:398 (1983)
10. Dalpiaz P. In *Proc. LEAR Workshop, 1st*, ed. H Poth. Karlsruhe: Kernforschungszentrum (1979)
11. Baglin C, et al. CERN Proposal CERN/ISRC/80-14, unpublished (1980)
12. Bharadwaj V, et al. Fermilab Proposal P760, unpublished (1985)
13. Baglin C, et al. *Nucl. Phys.* B286:592 (1987)
14. Henrichsen KN, De Jonge MJ. Report CERN/ISR/RF/MA 74-21 (1974); Montague BW. In *Theoretical Aspects*

of the Behaviour of Beams in Accelerators and Storage Rings, ed. MH Blewett, CERN Rep. 77-13, p. 63. Geneva: CERN (1977)
15. Macrí M. In *Antiprotons for colliding beam facilities: Proc. 1983 CERN Accel. Sch.,* ed. P Bryant, S Newman (CERN 84-15), p. 469 (1984)
16. Chattopadhyay S. In *AIP Conf. Proc. 127: Phys. High Energy Accel.,* ed. M Month, PF Dahl, M Dienes. New York: AIP (1985)
17. Brom J-M. *Formation des Etats Charmonium dans le Canal Direct d'Annihilation* $p\bar{p}$ *et Description d'une Methode Experimentale Nouvelle. Reactions Exclusives* $p\bar{p} \rightarrow e^+e^-$. PhD thesis. CRN, Strasbourg (1985)
18. Peoples, Jr. J. In *Proc. Workshop Design Low Energy Antimatter Facil.,* ed. D Cline, p. 144. Singapore: World Scientific (1986)
19. Tollestrup AV, Dugan G. In *AIP Conf. Proc. 105: Phys. High Energy Accel.,* ed. M Month, New York: AIP (1983); Petter J, et al. In *Proc. 1989 IEEE Part. Accel. Conf.,* 1:648 (1989)
20. Hikasa K, et al. (Particle Data Group). *Phys. Rev* D45:S1 (1992); erratum 46: 5210 (1992)
21. Armstrong TA, et al. *Phys. Rev.* D47: 772 (1993)
22. Rosen J, private communication
23. Due to SY Hsueh, private communication
24. Kennedy DC. *Phys. Rev.* D46:461 (1992)
25. Armstrong TA, et al. *Phys. Rev. Lett.* 70:1212 (1993)
26. Baglin C, et al. *Phys. Lett.* B163:400 (1985)
27. Lepage GP, Brodsky SJ. *Phys. Rev. Lett.* 43:545 (1979); Lepage GP, Brodsky SJ. *Phys. Rev.* D22:2157 (1980)
28. Feldman GJ. In *Proc. Int. Conf. High Energy Phys., 19th,* ed. S Homma, M Kawaguchi, M Miyazawa, p. 777. Tokyo: Phys. Soc. Japan, (1978)
29. Baglin C, et al. *Phys. Lett.* B172:455 (1986)
30. Oreglia MJ. *A Study of the Reaction* $\psi' \rightarrow \gamma\gamma\psi$. PhD thesis. Stanford University, Stanford, SLAC Rep. 236 (1980)
31. Armstrong TA, et al. *Nucl. Phys.* B373:35 (1992)
32. Armstrong TA, et al. *Phys. Rev. Lett.* 68:1468 (1992)
33. Armstrong TA, et al. *Phys. Rev.* D48: 3037 (1993)
34. Baglin C, et al. *Phys. Lett.* B195:85 (1987)
35. Oreglia M, et al. *Phys. Rev.* D25:2259 (1982)
36. Armstrong TA, et al. *Phys. Rev. Lett.* 69:2337 (1992)
37. Baglin C, et al. *Phys. Lett.* B171:135 (1986)
38. Gaillard MK, et al. *Phys. Lett.* B110: 489 (1982)
39. Armstrong TA, et al. FERMILAB-Pub-94/042-E Batavia: Fermilab. To be submitted to *Phys. Rev. D* (1994)
40. Baglin C, et al. *Phys. Lett.* B187:191 (1987)
41. Chen W-Y, et al. *Phys. Lett.* B243:169 (1990)
42. Aihara H, et al. *Phys. Rev. Lett.* 60: 2355 (1988)
43. Berger Ch, et al. *Phys. Lett. B* 167:120 (1986)
44. Braunschweig C, et al. *Z. Phys.* C41: 533 (1989)
45. Križan P, et al. In *Proc. 1991 Joint Int. Lepton Photon Symp. Europhys. Conf. High Energy Phys.* ed. S Hegarty, K Potter, E Quercigh, p. 92. Singapore: World Scientific (1992)
46. Adriani O, et al. *Measurement of* η_c *Production in Untagged Two-Photon Collisions at LEP.* CERN PPE 93-173. Submitted for publication in *Phys. Lett. B* (1994)
47. Kwong W, et al. *Phys. Rev.* D37:3210 (1988)
48. Ackleh ES, Barnes T, *Phys. Rev.* D45: 232 (1992)
49. Barnes T. In *Int. Workshop Photon-Photon Collis., 9th,* ed. DO Caldwell, HP Paar, p. 263. Singapore: World Scientific (1992)
50. Armstrong TA, et al. *Phys. Rev. Lett.* 70:2988 (1993)
51. Uehara S, et al. *Phys. Lett.* B266:188 (1991)
52. Lee RA. *Radiative Decays of the* ψ' *to All-Photon Final States.* PhD thesis. Stanford University, Stanford, SLAC Rep. 282 (1985)
53. Yamada S. In *Proc. 1977 Int. Symp. Lepton Photon Interact. High Energy,* ed. F Gutbrod, p. 69 Hamburg: DESY (1977)
54. Bodwin GT, Braaten E, Lepage GP. *Phys. Rev.* D46:1914 (1992)
55. Edwards C, et al. *Phys. Rev. Lett.* 48: 70 (1982)
56. El-Khadra AX, et al. *Phys. Rev. Lett.* 69:729 (1992)
57. Lucha W, Schöberl FF, Gromes D. *Phys. Rep.* C200:127 (1991)
58. Grosse H. *Phys. Lett.* B68:343 (1977); Martin A. CERN-TH.6933/93 To ap-

pear in *30th Course Int. Sch. Subnucl. Phys., Erice, 1992.*
59. Michael C. *Phys. Rev. Lett.* 56:1219 (1986)
60. Gromes D. *Z. Phys.* C11:147 (1981); erratum 14:94 (1982)
61. Eichten E, Feinberg F. *Phys. Rev.* D23:2724 (1981)
62. Brodsky SJ, Lepage GP. *Phys. Rev.* D24:2848 (1981); Andrikopoulou A. *Z. Phys.* C22:63 (1984); Berger EL, Damgaard PH, Tsokos K. *Nucl. Phys* B259:285 (1985)
63. Anselmino M, et al. *Phys. Rev.* D38: 3516 (1988)
64. Novikov VA, et al. *Phys. Rep.* C41:1 (1978)
65. Gottfried K. *Phys. Rev. Lett.* 40:598 (1978); Yan T. *Phys. Rev.* D22:1652 (1980)
66. McClary R, Byers N. *Phys. Rev.* D28: 1692 (1983)
67. Chao K, et al. *Phys. Lett.* B301:282 (1993)
68. Voloshin MB. *Sov. J. Nucl. Phys.* 43: 1011 (1986)
69. Kuang Y, et al. *Phys. Rev.* D37:1210 (1988)
70. Brodsky SJ, Lepage GP, Mackenzie PB. *Phys. Rev.* D28:228 (1983)
71. Olsson MG, Martin AD, Peacock AW. *Phys. Rev.* D31:81 (1985)
72. Lichtenberg DB, Potting R. *Phys. Rev.* D46:2150 (1992)
73. Gupta SN, Radford SF, Repko WW. *Phys. Rev.* D34:201 (1986); Pantaleone J, Tye S-HH, Ng YJ. *Phys. Rev.* D33: 777 (1986)
74. Halzen F, et al. *Phys. Rev.* D47:3013 (1993)
75. Cester R, et al. Fermilab proposal P835, unpublished (1990); Armstrong TA, et al. Fermilab proposal P835 (revised), unpublished (1992)